3D fabric reconstruction and image processing for clays
New method using SEM-FIB technique and AI

Myouri, Ismail; Bennai, Fares; Guyon, Julien; Hattab, Mahdia

DOI
10.1016/j.clay.2025.107943

Publication date
2025

Document Version
Final published version

Published in
Applied Clay Science

Applied Clay Science 276 (2025) 107943

Contents lists available at ScienceDirect

Applied Clay Science

journal homepage: www.elsevier.com/locate/clay

Research Paper

3D fabric reconstruction and image processing for clays - New method using SEM-FIB technique and AI

Ismail Myouri [a,b], Fares Bennai [a,*], Julien Guyon [a], Mahdia Hattab [a]

[a] Université de Lorraine, CNRS, Arts et Métiers Institute of Technology, LEM3, F-57000 Metz, France
[b] Section of Environmental Fluid Mechanics, Department of Hydraulic Engineering, Faculty of Civil Engineering and Geosciences, Delft University of Technology, 2628 CD Delft, the Netherlands

ARTICLE INFO

Keywords:
Clay behaviour
Clay microstructure
Focus Ion Beam (FIB)
Scanning electron microscope (SEM)
Curtain effects
Machine learning (ML)

ABSTRACT

This paper proposes a new technique for the 3D identification of clay particle orientations using images obtained from FIB-SEM observations. The method is based on a three-dimensional reconstruction that combines the Focused Ion Beam abrasion technique and Scanning Electron Microscopy, applied to kaolinitic clay selected for this study. The clay was first subjected to one-dimensional compression up to a given stress level, after which microstructural observations were performed using a post-mortem approach.

A novel methodology using appropriate image processing was established for this purpose, allowing for a precise treatment of the obtained FIB-SEM images. The proposed methodology first involved removing "curtain effects" and "charging artefact", which are specific types of noise commonly associated with FIB-SEM images. Two methods were employed to address this issue and were compared to evaluate their effectiveness: the first method was based on Fourier Transformation and Total Variational Reconstruction, while the second used a stochastic approach formulated as a convex optimization problem. Subsequently, a machine learning technique was integrated to enhance the segmentation process of the images. The final stage of the methodology involved creating a 3D model by reconstructing the clay particles in their spatial configuration. This paper aims to demonstrate how the proposed 3D observation method enables the quantification of the structural organization of clay particles in space in relation to mechanical loading.

1. Introduction

Clay fabric properties and their evolution during mechanical loading represent one of the essential aspects for understanding the micro-mechanic behaviour of clayey materials. On the other hand, the fabric, described by clay particle orientations and pore network properties, needs to be related to interparticle forces of a physicochemical nature to fully define the clay microstructure (Hattab and Chang, 2015). For this purpose, experimental observations appear as a necessary and fundamental approach to address this aspect, and finally support micro-mechanical modeling. One can mention Mitchell (1956), who studied the microscopic changes in intact and remoulded clays under different loading paths using optical microscopy. The author emphasized that the fabric formed in undisturbed and remoulded clays can be explained in terms of interparticle forces and history of the material subsequent to deposition and remoulding. The role of fabric in influencing the geotechnical properties of soils was clearly highlighted, as well as its impact on geotechnical structures, even at the field scale.

Several studies have been conducted using different observation techniques to analyze fabric at the micro and *meso* scales. One may cite observations performed using Scanning Electron Microscopy (Sloane, 1966; Pusch, 1970; Diamond, 1971; Yoshinaka and Kazama, 1973; Hicher et al., 1994, 2000; Al-Rawas and McGown, 1999; Mitchell and Soga, 2005; Hammad et al., 2013; Ma et al., 2025), X-ray tomography (Birmpilis et al., 2017; Gao et al., 2020b; Nishimura et al., 2020; Fan et al., 2021; Birmpilis et al., 2022), Transmission Electron Microscopy (Pusch, 1970; Murphy et al., 1977; Laribi et al., 2005; Gaboreau et al., 2016; Liu et al., 2019), X-ray diffraction (Diamond, 1971; Yoshinaka and Kazama, 1973; Martin and Ladd, 1975; Souli et al., 2010), Mercury Intrusion Porosimetry (MIP) (Delage and Lefebvre, 1984; Griffiths and Joshi, 1989; Simms and Yanful, 2004; Tarantino and De Col, 2008; Hammad et al., 2013; Pedrotti and Tarantino, 2018), and more recently, Small-Angle X-ray Scattering (SAXS) (Hubert et al., 2013; Asaad et al., 2021; Fang et al., 2021). Among these works, Morgenstern and

* Corresponding author.
E-mail address: fares.bennai@univ-lorraine.fr (F. Bennai).

https://doi.org/10.1016/j.clay.2025.107943
Received 11 August 2024; Received in revised form 22 July 2025; Accepted 24 July 2025
Available online 31 July 2025

Tchalenko (1967) used polarized light microscopy and the birefringence technique on kaolin specimens subjected to direct shear. They observed a strong orientation of particles in the direction of movement, accompanied by kink-bands. Pusch (1970) focused on the behaviour of a highly sensitive marine clay under unconfined compression. Micrographs highlighted microstructural changes and particle group movements as a result of shear deformations. On artificial cohesive soil composed of sand, silt and clay, Cetin and Söylemez (2004) identified reorientation mechanism of the particles, pores, and other constituents during both drained and undrained direct-shear tests. The quantification of fabric changes was conducted through petrographic observations at various distances from the failure planes formed at different shear displacements.

Post-mortem analyses using SEM observation techniques have proven to be effective in obtaining qualitative and semi-quantitative information on clay particle orientations. Most of the research conducted in this area aims to establish a link between mechanical loading paths and fabric evolution at the microstructural scale. For instance, under one-dimensional compression (applied to the clay specimen), particles tend to align horizontally, perpendicular to the loading direction (Hammad et al., 2013; Cotecchia et al., 2016; Chow et al., 2019). In contrast, isotropic loading induces a random orientation of the particles (Sivakumar et al., 2002; Hattab and Fleureau, 2011; Gao et al., 2020a). On saturated reconstituted clay subjected to triaxial loading paths, Hattab and Fleureau (2010), Hattab and Fleureau (2011) and, more recently, Gao et al. (2020a) demonstrated how the phenomenological dilatancy behaviour can be linked to relevant local mechanisms.

However, using SEM technique means investigating a given surface trimmed from a specimen after mechanical loading. Thus, fabric information is obtained from 2D observations, which represents a limitation that must be considered when interpreting the results. Among recent promising techniques one can mention Focused Ion Beam (FIB) coupled with Scanning Electron Microscopy (SEM), which enables the reconstruction of a 3D model from images of a given material. Over the last decade, this technique has been widely used, showing its efficiency in observing pore networks in materials such as claystones (Keller et al., 2011; Hemes et al., 2016; Laurich et al., 2017) and cementitious materials (Holzer et al., 2006; Lim et al., 2018; Song et al., 2019). On the other hand, the FIB-SEM technique is considered one of the most effective three-dimensional observation methods for nanopore imaging, unlike X-ray tomography, which is limited by voxel size. Using FIB-SEM, Zhou et al. (2016) characterized pores in shale from the Longmaxi formation and classified them into three types: organic pores, inorganic pores, and microfractures. Furthermore, Faÿ-Gomord et al. (2017) successfully reconstructed the pore network of chalk rocks using FIB-SEM imaging, allowing them to quantify the size and shape of the pores. However, FIB-SEM technique has rarely been used in soils such as soft clays, remoulded clays, mud, or clay slurries. Indeed, these materials present several challenges that can affect the effectiveness of image analysis and processing. One of these challenges is the systematic presence of the “curtain effect” noise, which appears as a distinct topographical imprint with line-like pattern due to FIB cutting (Hemes et al., 2015; Spehner et al., 2020). Other issues arise during the image segmentation stage, particularly in the separation of pores from particles, initiated in the works of Ding et al. (2024), Bennai et al. (2025a) and Bennai et al. (2025b). In this regard, machine learning approaches appear to be a promising solution to this problem, demonstrating their effectiveness in providing powerful tools for solving challenges that may arise in various fields of geomechanics (Ghaboussi et al., 1991; Ellis et al., 1995; Moayedi and Hayati, 2018; Ma et al., 2022). Additionally, numerous studies have demonstrated the application of machine learning techniques in predicting the dynamic properties and characteristics of granular mixtures (Manafi Khajeh Pasha et al., 2019; Das and Chakrabortty, 2022), predicting the soil compaction parameters (Benbouras and Lefilef, 2023), and modeling the behaviour of granular materials (Ma et al., 2022). In image processing, machine learning is widely used in the medical field to identify biological cells and analyze radiographs (Bordigoni et al., 2024; Jiang et al., 2025), as well as in materials science. For example, it has been employed to study the porosity of porous polymers (Čalkovský et al., 2021), and to identify and analyze corrosion of steel-reinforced concrete (Xin et al., 2024). Aiming to enhance the quality of microstructural investigations in clays by accurately quantifying fabric properties in relation to mechanical loading, we focus on the use of Machine Learning techniques, particularly for image processing, while addressing challenges associated with FIB-SEM images.

Using the FIB-SEM technique on a microvolume of clay at a given state, one may reconstruct the clay’s structure in three dimensions. The slices used for this reconstruction are usually affected by curtain effects and charging artifacts, which has to be removed using an appropriate method. The curtain effect appears as parallel vertical scratches with varying intensities. According to Giannuzzi and Stevie (1999), Giannuzzi and Stevie (2005) and Lemmens et al. (2011), this effect represents real surface topography caused by variations in FIB milling rates due to local differences in the sample’s hardness. Consequently, curtain effect lines are typically aligned with the ion beam milling direction. Another type of noise that appears in FIB-SEM images is caused by charging artifacts, which occur when the energetic electron beam interacts with highly insulating regions. Charging artifacts manifest as spots with asymmetric streaks in the horizontal direction (Dumoux et al., 2023). The presence of these two types of noise (curtain effects and charging artifacts) in the images can significantly affect the quality of microstructural quantification after image processing. For instance, it has been observed that curtain noise can be mistakenly identified as clay particles during the segmentation phase.

Current techniques, such as those presented by Giannuzzi and Stevie (2005) on various materials (e.g., alloys and plated ceramic structures), Lemmens et al. (2011) on shale, or Loucks et al. (2012) on mudrocks, mainly focus on eliminating the curtain effect during the image acquisition stage. The main challenge in observing soft, mud, or remoulded clays is that FIB-SEM output data, even after acquisition, generally remain contaminated with curtain noise, requiring additional image processing.

The method proposed by Schwartz et al. (2019) aimed to eliminate the “curtain effect” by identifying its signature in Fourier domain and then recovering the missing wedge information using total variation minimization, relying on image sparsity-based reconstruction techniques. This approach was applied to various materials, including pearl and InGaN nanowires. Fehrenbach et al. (2012) proposed a method based on a stochastic approach formulated as a convex optimization problem, which can be solved numerically. The applications of this method were diverse, including images of branchial arches, images of a region of a multicellular tumor spheroid, and examples of images taken from toys.

In this paper, we address a significant research gap in the analysis of the microstructure of clay soils by proposing a comprehensive approach that integrates observation, image denoising, particle identification using artificial intelligence (AI), and the quantification of their orientations. This approach evaluates and compares both denoising methods mentioned above, applying them to clayey soil to determine the most efficient method for preserving the microstructural details of clay.

The originality of this study lies in the integration of an artificial intelligence model for the image segmentation process, enhancing the accuracy of particle detection and separation compared to conventional methods, which have shown limitations in identifying the shapes of a stacked kaolinite particles in 3D. These particles, which can be approximated as rigid planes, are characterized by their specific spatial orientations. By applying principal component analysis (PCA), we precisely determine the coordinates of the points defining each particle-plane and subsequently characterize their orientation through the normal vector. The proposed method ultimately allows for the identification of clay fabric in space through the orientation of the normal

vectors.

2. Material and techniques

2.1. Material properties and terminology

The studied synthetic clay, from Sibelco company (France), is a Kaolin containing high percentage of kaolinite faction. Kaolinite particles exhibit a relatively regular hexagonal plate-like shape. Atterberg tests revealed a Plastic Limit (w_P) of 20 % and a Liquid Limit (w_L) of 40 %, with a specific weight of 26.3 kN/m^3. X-ray diffraction analysis conducted by Cheng et al. (2021) identified kaolinite as predominant mineral of the clay (over 90 %), with a small presence of quartz (less than 10 %) and traces of illite. Fig. A11 shows SEM photo of the material used in this study, where one can clearly observe the kaolinite particles presenting themselves as a plate-like shape.

To prepare the tested specimen, dry clay powder was first mixed with demineralized water up to initial water content of $w_0 = 1.5w_L$. The resulting slurry was introduced layer by layer into a consolidometer of double drainage so that the material can be sedimented, and then subjected to a one-dimensional compression with vertical effective stress of $\sigma'_v = 120$ kPa. This method for preparing consolidated clayey soil, suggested by Biarez and Hicher (1994), has proven efficient and has been used for decates (Hattab and Hicher, 2004; Hammad et al., 2013; Zhao et al., 2019). Thus, a consolidated saturated clay core was obtained from which different samples can be trimmed for micro-observations. Parallelepiped sample measuring 5 × 5 × 15 mm^3 was carefully cut from the specimen that had been subjected to mechanical loading, and was well referenced with respect to the mechanical loading (especially the stress direction). The sample thus prepared was fully saturated; however, SEM observation technique requires the material to be dry with pores completely free of water. Therefore, the lyophilization process suggested by Delage and Pellerin (1984) was adopted to preserve clay's microstructure during drying before introducing it in the FIB-SEM chamber. This method consists first to freeze the liquid water in the pores by immersing the sample in liquid nitrogen. The sample is then fractured along the middle plane to obtain two sub-samples measuring 5 × 5 × 7.5 mm^3 each. Subsequently, ice sublimation into water vapor (for water extraction) was performed using freeze-dryer cell. Afterwards, the sub-sample was affixed to a scanning electron microscope (SEM) support with deposition of layers of gold and carbon on the upper face of the sub-sample. Notice that the latter face was identified as perpendicular to the stress axis. The gold and carbon layers aimed to enhance the conductivity of the material and minimize electron charging effects.

2.2. FIB–SEM technique

In this study, The Zeiss Auriga dual beam system, which combines Focused Ion Beam (FIB) and Scanning Electron Microscopy (SEM), was used for the 3D observation of the clay microstructure. Notice that the inclination angle between the ion and electron beams was set at 54 degrees.

The sub-sample was placed inside the FIB-SEM chamber and the area of interest was located, three protective layers (each approximately 0.5 to 1 µm thick) of platinum "Pt", carbon "C", and platinum "Pt" again, were deposited on the metallized surface of the sub-sample. Subsequently, several steps described in Fig. B. 12 were followed to prepare and observe the area of interest:

- Using Focused ion beam (FIB), holes were dug on the sub-sample surface, then further excavate to isolate a micro-volume as can be observed in Fig. B. 12a. This micro-volume was maintained by two points on parallel lateral surfaces.
- The micro-volume was then welded to the nanomanipulator and can be separated from the sub-sample (Fig. B. 12b).
- Fig. B. 12c shows the micro-volume extracted and deposited on a copper grid
- To measure the thickness of the slices and ensure accurate image alignment for a fine 3D microstructure reconstruction at the end of acquisition, five sets of linear markers were milled by the ion beam on the platinum layer on the micro-volume's upper surface, and subsequently filled with carbon (Fig. B. 12d).

Images are acquired by SEM with an acceleration voltage of 2 kV, a probe current of 100 pA and 10 nm pixel size. Slices are milled by a FIB probe of 30 kV with 4 nA of current with a slice thickness of 10 nm. Both imaging and milling are done simultaneously, which enhances analysis stability and generates a stack of images along the X-axis as observed in Fig. 2a. Notice that abrasion of the slices by the FIB column was performed in the YZ plane, knowing that axial stress direction of the one-dimensional compression corresponds to Z axis. The metallized sub-sample surface corresponds to XY plane, which is perpendicular to the applied axial stress.

As mentioned in this paper, different kind of samples are defined at various scale, Table 1 is introduced for clarity, providing appropriate terminology for each sample.

3. Proposed image processing method for clays

After image acquisition, a stack containing approximately 2280 2D-SEM images, spaced 10 nm apart, was obtained and aligned into perfectly parallels images (Fig. 1a). The observed micro-volume can be reconstructed from this stack of images representing successive sections. However, it may be noted that during the acquisition process, misalignment of the images can occur due to displacements and deformations caused by acquisition instability problems. Therefore, alignment correction is thus essential to accurately reconstruct a digital micro-volume (representing the geometrical configuration of the clay fabric) based on 3D representation from accurate positions of the successive 2D image. This necessary step of image alignment was performed according to Ding et al. (2024). Fig. 1b presents the result of the used method showing a 3D reconstruction of the observed micro-volume, visualized by AVIZO software. The reconstructed block here represents a volume of interest of 22 × 35 × 28 µm^3. A 3D median filter was then applied to reduce image noise.

3.1. Denoising approaches for images

In this study FIB-SEM images were affected by bidirectional artifacts (curtaining and charging) appearing in the horizontal and vertical directions, as observed in Fig. 1b. These artifacts represent a real problem leading misinterpretation during the image processing stage, and this reverberates on the results of microstructure quantification. To correct

Table 1
Terminology Corresponding to samples dimensions.

Terminology	shape	Dimensions	Scale of the sample
Specimen	Cylindrical	D = 94 mm - H = 50 mm	*Used for macro laboratory test*
Sample	Parallelepiped	5 × 5 × 15 mm^3	*Cut from the specimen treated outside the FIB-SEM cell*
Sub-sample	Parallelepiped	5 × 5 × 7.5 mm^3	*Block cut from the sample and then introduced in the FIB-SEM cell and retreated again for imaging*
Micro-volume	Parallelepiped	38 × 35 × 45 µm^3	*Cut from the subsample*
Digital Micro-Volume	Parallelepiped	38 × 35 × 45 µm^3	*Digital 3D reconstruction*

The protocol needs to perform different sampling, from the macro mechanical test to the micro 3D reconstruction. Table 1 has been introduced as guide for the reader to distinguish between them through these different terminologies.

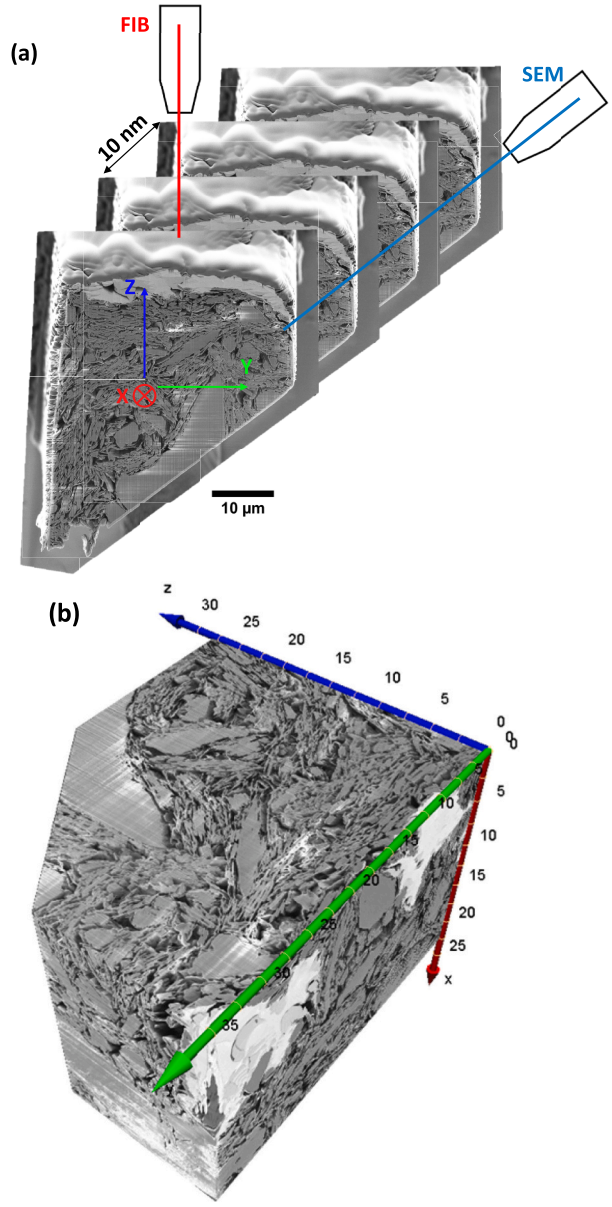

Fig. 1. FIB-SEM Observation: (a) Alternating operation of the focused ion and electron beams, (b) 3D reconstruction of the clay micro-volume 22 × 35 × 28 µm3 of dimensions

curtain effect and charging artifacts noise, we propose filtering methods based on the following criteria:

- Preserving the quality of the processed image without introducing additional artifacts that could lead to misinterpretation during the segmentation phase.
- Considering the large number of images to be processed, the method must allow automated processing with minimizing operator intervention as much as possible.
- Requiring a reasonable processing time for each image.

Thus, in this purpose, two methods were used and compared to test their efficiency in curtain effect and charging artifacts removal: on the one hand a fast removal based on Fourier Transformation/Total Variation reconstruction, and on the other hand a powerful stochastic approach (named VSNR: Variational Stationary Noise Remover).

3.1.1. Fourier transformation and total variation reconstruction approach

It is generally accepted that the straightforward and efficient way to remove scratches from images of image sensing systems is to remove their representations in the Fourier Domain. It has been shown that aperiodic scratches extending in the vertical or horizontal direction occupy a wedge-shaped domain in the orthogonal direction to the original scratch direction, and they are confined in an angular range in Fourier space (Schwartz et al., 2019). Although removing this wedge domain gives a better visualization of the real object, the method can degrade the quality of the image by introducing additional complex streaks and blurry artifacts commonly known as "missing wedge artifacts". To overcome this difficulty, a Compressed Sensing technique named Total Variation (TV) minimization method was used by Schwartz et al. (2019), which makes it possible to recover missing structural information in Fourier space without restoring restricted scratches in the missing wedge.

The method described above was mainly developed for unidirectional scratches and strip noises, it is however possible to test its efficiency for two-directional type of noise, involving simultaneously vertical and horizontal scratches. To do this we developed a Python code to remove the wedge domain in Fourier space, and then reconstruct the image using the TV minimization method by solving the following optimization problem: $min\|\nabla\hat{x}\|_1$ such that $\Phi\hat{x} = b$. $\hat{x}$ and b represent the reconstructed (destriped) image and the measured data (acquired image) respectively. Φ is the measurement matrix, and ∇ transforms the image to the gradient-magnitude (sparse) domain (Qi et al., 2015; Schwartz et al., 2019).

To validate the proposed processing method, a simple object is taken as an example and illustrated in Fig. C. 13. One can observe in Fig. C. 13a an original image of a garnet (simple geometric shape), while Fig. C. 13b presents its Fast Fourier Transform (FFT). Subsequently, vertical bands comparable to curtain effects were manually added to the original image of Fig. C. 13a which gives Fig. C. 13c. Fig. C. 13d exhibits Fourier Transform of this noisy image. The difference between the two cases, ie without (Fig. C. 13b) and with (Fig. C. 13d) strips noise, is observed in the horizontal line at the center of the image mainly due to the added vertical strips. Fig. C. 13e results from the difference between the reference image and the noisy image, and can provide an interesting indication of the part added to the original image due to the introduction of the curtain effect. One can notice that the size of the object (garnet) or the spacing between the vertical added stripes are not key parameters for the applicability of the method.

The results obtained after the removal of the vertical strips are presented in Fig. C. 13. The effect of the vertical stripes on the FFT domain is eliminated by using a 30° wedge as represented in Fig. C. 14a, and then a reverse FFT is used to reconstruct the image as shown in Fig. C. 14b. This new reversed image is then compared to the original image of Fig. C. 13a and leads to significant artifacts caused by the elimination of the wedge in Fourier space. Fig. C. 14c highlights the difference between the original image (Fig. C. 13a) and the denoised image after wedge elimination in the Fourier domain (Fig. C. 14b). Finally, the Total Variation minimization technique is applied to denoised images (Fig. C. 14a and Fig. C. 14b) with artifacts to eliminate high incoherence (which is characteristic of artifacts generated by the wedge elimination technique). The reconstruction of the missing wedge in the Fourier Domain is performed and represented in Fig. C. 14d. The corresponding denoised image is presented in Fig. C. 14e, the difference between this new image and the original image (Fig. C. 13a) is given in Fig. C. 14 f. The FFT of the denoised image using both the wedge elimination and the Total Variation minimization shows the reconstruction of the missing wedge in the Fourier Domain that was eliminated when applying the wedge elimination technique. The FFT of the newly reconstructed photo can now be considered as similar enough to the original image. Note that this restoration induces a loss of image resolution, however, the main information restoring the shape of the garnet has been preserved.

To eliminate the curtain strips without significantly affecting the

overall image quality, an angle wide enough was chosen for the wedge filter in Fourier space. Wedge angles of α = 4°, 6°, and 8° were applied in both horizontal and vertical directions to the images, with different penalization values named p_n for the TV minimization algorithm. This allowed to satisfy the parameters values of the following combination (Eq.1).

$$\{(\alpha, p_n) |\ \alpha \in \{4, 6, 8\}\ and\ p_n \in \{0.1, 0.25, 0.4\}\ \} \quad (1)$$

α,p_n were chosen by comparing, visually, the quality of the reconstruction of all the images resulting from the combined parameters (Eq.1), the main goal here being to try to find an optimal compromise between reducing noises in the reconstruction and preserving the authentic signal. Indeed, a very high value allows to well reduce curtain strips but would also result in a loss of details and the merging of closely spaced elements. In our case, the optimal selected parameters are α=8° and a penalization term $p_n = 0.40$.

3.1.2. Stochastic approach

The second possible method consists in the Variational Stationary Noise Remover, which is a restoration and denoising algorithm based on a Bayesian approach.

In general, the observed digital image (denoted u_0) can be decomposed into two parts: a smooth original image part and a noise part, as expressed by Fehrenbach et al. (2012) in the following mathematical form (Eq. 2).

$$u_0 = \bar{H}u + b \quad (2)$$

Where u_0 is the observed digital image, u represents the denoised digital image, $\bar{H}$ is a deterministic linear operator representing the acquisition process (including sampling, convolution, indirect measurements, etc.), b represents the noise or texture.

This algorithm aims to provide as much as possible the best estimation of u and b, given the observed image u_0, taking into consideration the A Prior knowledge of the probability density function (p.d.f) of the desired values, in order to separate stripes from the image. The probability density function (p.d.f) of the noise b, is based on the "stationary noise assumption", which implies that the statistical properties of the noise are generally or locally preserved despite any translation. The p.d.f for the denoised image u is chosen in such a way as to promote the images that are smooth or piecewise smooth. Consequently, the problem can be mathematically formulated as a problem of convex optimization type known as Maximum A Posteriori (MAP) approach as expressed by Eq. 3, where p denotes the probability density function.

$$Find\ (u, b) \in argmaxp(u, b \| u_0) \equiv argmax\left(\frac{p(u_0 \| u, b) \times p(u, b)}{p(u_0)}\right) \quad (3)$$

The implementation of denoising method with the above approach was in this study meticulously performed using Python programming language.

Since a pre-existing library for VSNR denoising method performed by Fehrenbach et al. (2012) was already available with the original MATLAB code, we took an active approach to ensure the configuration and adaptability of the denoising process to our specific requirements concerning specifically the FIB-SEM images of clays.

For this work, the configuration step required four patterns with different dimensions set for each direction: horizontal direction and the vertical directions. On the other hand, denoising calculations were executed using the capabilities of a GPU (Graphics Processing Unit), which significantly reduced computation time. The algorithm showed thus a remarkable performance improvement. It has to be mentioned that in our study case, running the algorithm on an NVIDIA GeForce RTX 2080 Ti GPU decreased the calculation time from one hour per image, to just one minute per image, representing a significant time saving.

3.1.3. Results of processing and discussion

Fig. 2a presents a FIB-SEM slice of the micro-volume before image processing. Examples of curtain effects are highlighted with red arrows. Fig. 2b presents the treatment results after Fourier Transformation and Total variation reconstruction method for removing curtain effects in FIB-SEM images. One can observe that the method appears rather effective in eliminating unidirectional strip noise but fails in the bidirectional strip noise treatment. Despite using the Total Variation algorithm to reconstruct the missing wedge in Fourier space, we noticed that some artifacts remained apparent and were not fully removed. For bidirectional strips noise (curtain effect and charging artifacts), one can observe a degradation of image quality after FT processing, even if small wedge area in Fourier space was removed. Two degraded zones are highlighted in red in Fig. 2b. This degradation is linked to the FT method itself when applied to complex image noises, such as those present in these kinds of clay images, which required removing two wedge areas. It is therefore not realistic in this approach to consider eliminating curtain effects without deeply compromising the image quality.

Regarding the Variational Stationary Noise Remover (VSNR) tool, the image processing using our Python-implemented algorithm leads to results presented in Fig. 3. VSNR appears as powerful tool for the curtain effect denoising. Using this stochastic approach allowed to obtain a more satisfactory image correction with a significantly superior quality compared to that obtained from the combined Fourier Transformation and Total Variation reconstruction method. This stochastic approach is much more relevant as it effectively removes all curtain effect noise while preserving the quality of the original image (Fig. 3a) as one can observe in Fig. 3b. Based on the results of the two methods, the stochastic approach using the VSNR tool was selected as more efficient for image processing aiming to identify the clay particles.

However, it is important to note that there are some limitations to the method. Firstly, to ensure reasonable processing times for denoising, processing of large stacks of images requires powerful computing device equipped with a fast GPU. Secondly, finding adequate and optimal parameter settings can be challenging. Indeed, some images may remain unprocessed if the *penalization* term is taken too large but may be also dramatically damaged if the penalization term is taken too small. Therefore, additional processing cycles need to be launched with modified settings for these images. This means that the calculation will be run again for the processing of these images with adjusted the penalization parameter. Another limitation that may appear is related to the influence on the processing results of slight differences between some image slices in terms of image quality and luminosity. This point requires special attention, as it can affect the segmentation process and the selection of images for machine learning-based image segmentation.

3.2. New segmentation methodology for FIB-SEM images using machine learning approach

After curtain effect and charging artifacts removal from FIB-SEM images the following step consists of particle identification, the main objective being to capture information from appropriate reconstruction of the FIB-SEM images allowing to determine the spatial orientations of clay particles. To achieve this, the method that we used required to simplify the digital 3D image by identifying the two phases constituting the clay fabric, i.e., the pores on one hand and the particles on the other hand. Thus, digital images were segmented and decomposed into multiple regions regrouping voxels recognized as solids (clay particles or silica grains) and those of recognized as pores. The latter process, named image segmentation, represents one of the first stages of image processing.

Usually, on 2D SEM images segmentation process was carried out using different methods including the manual one. Manual segmentation can be enough precise but obviously extremely tedious, time-consuming. It therefore appears with strong limitations to analyze the complete FIB-SEM dataset as numerous segmented images typically

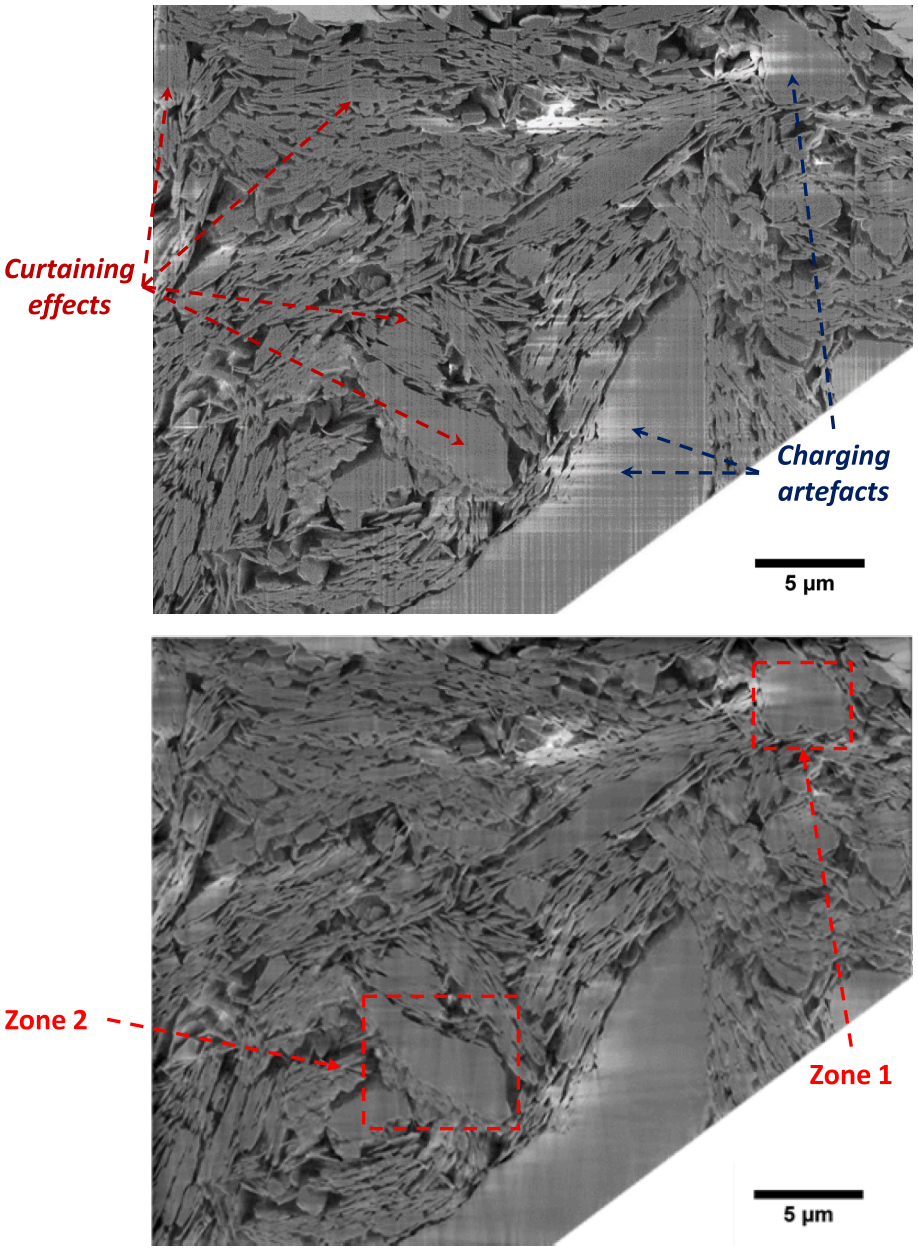

Fig. 2. Curtain effect correction - Fourier Transformation and Total variation reconstruction approach.
a Original FIB-SEM image containing curtain effects.
b Treated Image with Fourier Transformation and Total variation reconstruction approach

required to generate a 3D image from 2249 2D images. Automatic and semi-automatic image analysis methods for 2D SEM images have been proposed using simple thresholding techniques (Gao et al., 2020b; Zhao et al., 2020; Nyo et al., 2022; Singh et al., 2022). The issue to use these approaches is that they generally fail to detect clay particles with acceptable accurately, especially when particles are associated in aggregates or form complex clusters. This main difficulty of automatic methods to well identify the particles is reflected in the analysis of spatial orientations of the particles.

This challenging problem is addressed in this work by using machine learning methodology especially adapted for image segmentation. Machine learning algorithms are able to learn efficiently from their training using a large number of examples showing how different objects in the clay fabric should be detected. Then, the algorithms become capable on their own of automatically identifying and classifying the different phases within the images. Thus, by training the algorithm on a carefully labeled dataset, it becomes possible to automate the segmentation process, and significantly reduce potential errors linked to particles identification stage.

Machine learning-based approaches is precisely showed in Fig. 4a presenting a photo of a Biarez and Hicher (1994) thesis manuscript taken from the edge. Then, two different approaches were used aiming to try identifying the leaves with enough accuracy. This example illustrates leaf-shaped objects, to be identified, resembling to clay particles. The first approach involves "Threshold-Based Segmentation," which segments the image based on the intensity of each pixel (Fig. 4b). Furthermore, after applying the watershed algorithm, it becomes failing to accurately identify individual leaves of the manuscript. Figs. 4c shows that when leaves, as clays particles, are in contact with each other, they are often identified as an assembly of leaves (ie particles). These results being not conclusive, it was therefore crucial to seek a more advanced and reliable method for image segmentation. Fig. 4d illustrates the

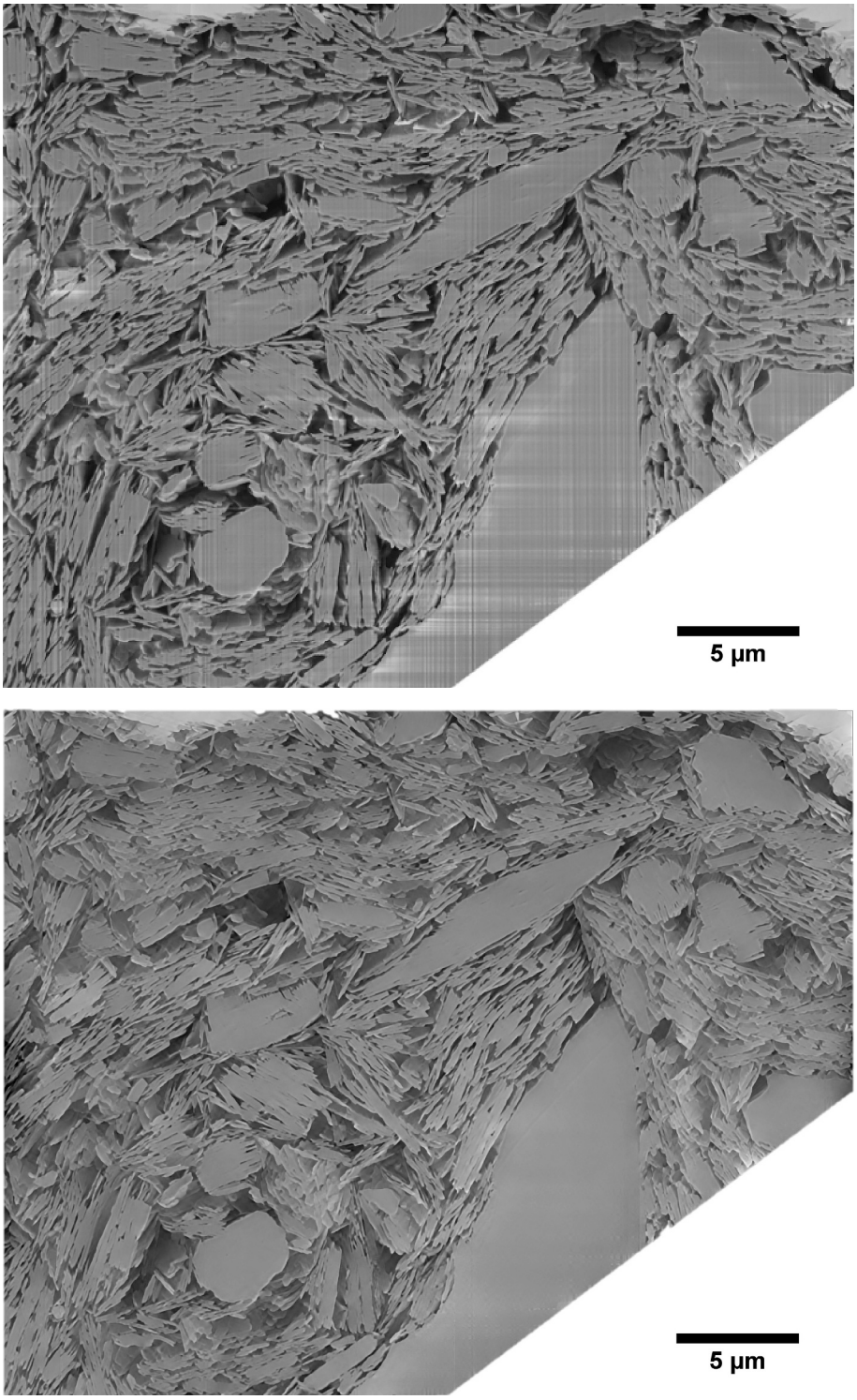

Fig. 3. Curtain effect correction - Result using VSNR filter-based processing approach
a Original FIB-SEM image containing curtain effects
b Treated Image with VSNR filter-based processing approach

segmentation result achieved through machine learning, and show very clearly leaves well separately reproduced after training the model with a probability greater than 90 % that the identified objects are leaves shown by red line. After that, each paper is then detected individually by selecting the bounded red objects from the machine learning method that have a size in the range of reality using the segmentation plugin for particle analysis in ImageJ. The method successfully identifies the majority of the manuscript leaves accurately. Hence, this approach appears as quite well accurate to be used in the present study for the identification of clay particles.

Ilastik software was used to select multiple images for the training process. During this operation, one may observe that using images by clearly distinguishing the different fraction of the clay microstructure have highly improved the quality of the training. For segmentation

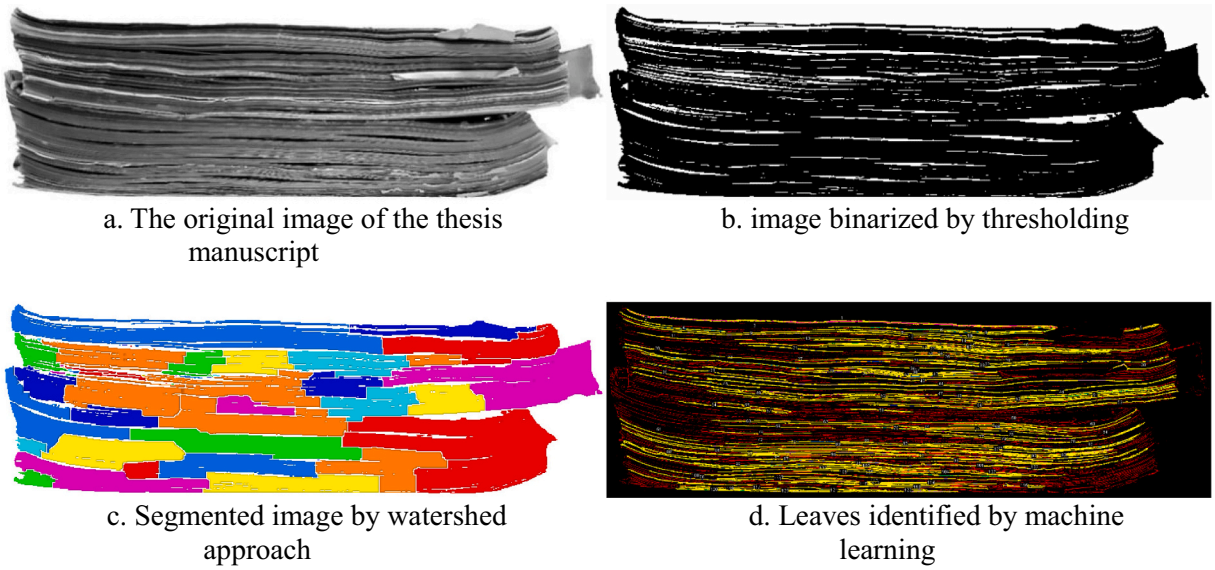

Fig. 4. Example of the power of AI for identifying sheet objects based on Biarez and Hicher (1994) thesis dissertation.
a The original image of the thesis manuscript
b image binarized by thresholding
c Segmented image by watershed approach
d Leaves identified by machine learning

configuration three classes of features were created: i- clay particles, ii- silica grains, and iii- pore space. Numerous examples were provided as input for the classifier within each class, using the training images. The trained model developed in this study, to be applied to the kaolin clay, was progressively enriched by providing systematic corrections whenever misinterpretations were detected during the process of the model phase identification. Once the model produced satisfactory results, the classifier can be applied to the entire FIB-SEM image data to obtain probability map of each class, which indicates whether a specific region of interest (selected region on the reconstructed digital photo) exceeds (or not) a predetermined threshold value (Tv). The resulting probability map indicates the probability that each pixel belongs to a given class. The threshold value (Tv) is used to convert this probability map into a binary image. This threshold distinguishes pixels belonging to the object from those that do not. The higher the Tv, the more likely it is that the selected pixels truly belong to the object. In our case, Tv was set to 95 %, meaning only regions with a high probability (greater than or equal to 95 %) of containing significant clay particle fractions were selected.

4. Novel quantitative method characterization clay fabric properties

4.1. 3D identification of particle plane and orientation

Knowing that the thickness of the kaolinite particle is much smaller than its surface dimensions, each platelet of the clayey fabric can be assimilated to a plane with a given orientation in space. One can consequently assume that the particle orientation can be represented by the orientation of the normal vector to its surface. The challenge in this section is to define the more adequate plane that may represent the associated particle belonging to the digital reconstructed volume.

The main idea here is to define a given particle plane from their discrete cloud formed by material points taken on the digital particle. Then, the problem can be simplified since it becomes enough to find the best-fit plane that satisfies the distribution of the dot cloud, and then to define the normal vector to this plane and its orientation in the space.

To do this we propose a calculation method for 3D fitting of particle planes, based on Principal Component Analysis (PCA) which is commonly used as a dimensionality-reduction tool in exploratory data analysis. This method, analogous to linear regression, involves searching for the plane that minimizes the average (mean-squared) distance between the original vectors and their projections onto the searched plane. This method allows to fit a distribution of dots to the plane (Fig. 5a and Fig. 5b). The direction of a plane can also be described using two non-zero non-collinear vectors, alternative approach consists in defining two orthogonal projections along two axes where the mean average distances between the original vectors and their projections on each of those orthogonal axes are minimal. The two axes tend to correspond to the orthogonal directions with the maximum variances of the position vector projections (Shalizi, 2013). Solving this problem involves finding the axis of maximum variance in a set of data, which can be achieved using PCA method.

Based on this approach, the developed algorithm uses PCA method on the point cloud coordinates to determine their principal axes from the spatial geometry of all the detected clay particles of the FIB-SEM images. Subsequently, one may calculate the best-fitting plane and its orientation.

In summary, the developed algorithm follows the main outlined steps below.

First, the coordinate matrix (X_{ij}), representing the voxels belonging to the clay particle, was used to compute the centroid matrix (X_{cij}), which allows to calculate the covariance matrix.

$$X_{ij} = \begin{pmatrix} x_{11} & x_{12} & x_{13} \\ x_{21} & x_{22} & x_{23} \\ \vdots & \vdots & \vdots \\ x_{n1} & x_{n2} & x_{n3} \end{pmatrix}, X_{cij} = \begin{pmatrix} x_{11}-\overline{x_1} & x_{12}-\overline{x_2} & x_{13}-\overline{x_3} \\ x_{21}-\overline{x_1} & x_{22}-\overline{x_2} & x_{23}-\overline{x_3} \\ \vdots & \vdots & \vdots \\ x_{n1}-\overline{x_1} & x_{n2}-\overline{x_2} & x_{n3}-\overline{x_3} \end{pmatrix} \quad (4)$$

In Eq. 4 $\overline{x_j}$ represents the mean value of the column vector j. The covariance matrix can then be computed using the quadratic form of X_c: $Cov(X_c) = \frac{1}{n} X_c{}^t X_c$.

To solve this problem, the covariance matrix was decomposed into

a. Example of clay particle obtained by image processing

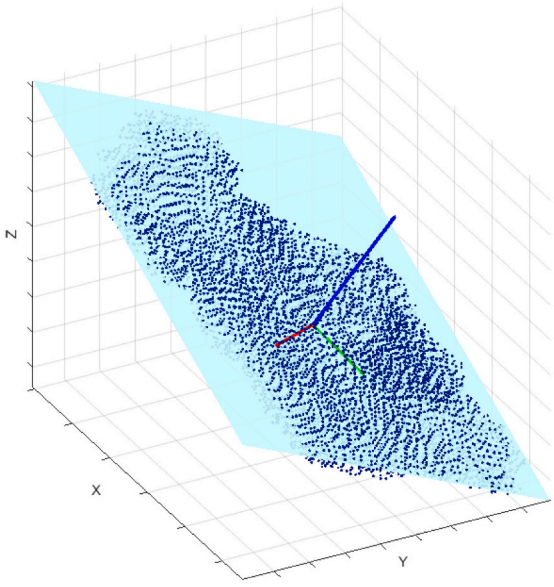

b. PCA method for the identification of particle's plane and its axes

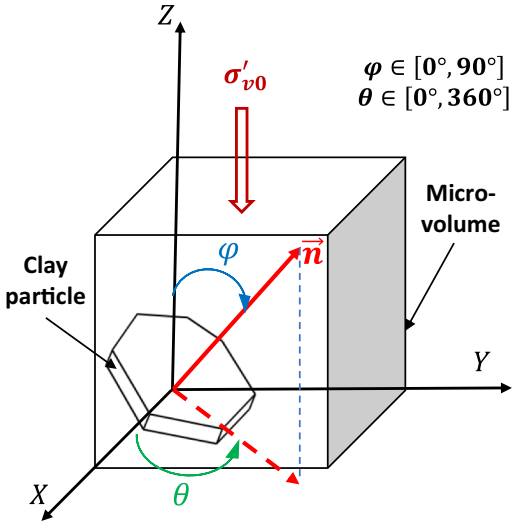

c. Representation of the normal vector orientation using φ and θ

Fig. 5. Clay particle reconstruction using the PCA method. Plane fitting process and its normal vector. Local coordinate system representation of a clay particle
a Example of clay particle obtained by image processing
b PCA method for the identification of particle's plane and its axes
c Representation of the normal vector orientation using φ and θ

its principal orthogonal directions or eigenvectors V_1 (v_{1x}, v_{1y}, v_{1z}), V_2 (v_{2x}, v_{2y}, v_{2z}), and V_3 (v_{3x}, v_{3y}, v_{3z}), along with the corresponding eigenvalues of the particle are $\lambda_1 \geq \lambda_2 \geq \lambda_3$.

$$Cov(X_c) = \begin{pmatrix} v_{1x} & v_{2x} & v_{3x} \\ v_{1y} & v_{2y} & v_{3y} \\ v_{1z} & v_{2z} & v_{3z} \end{pmatrix} \begin{pmatrix} \lambda_1 & 0 & 0 \\ 0 & \lambda_2 & 0 \\ 0 & 0 & \lambda_3 \end{pmatrix} \begin{pmatrix} v_{1x} & v_{1y} & v_{1z} \\ v_{2x} & v_{2y} & v_{2z} \\ v_{3x} & v_{3y} & v_{3z} \end{pmatrix} \tag{5}$$

The two principal components named V_1 and V_2 define the fitted plane, while V_3, the third principal component, represents the normal to the plane. The orientation of the clay particle is expressed by the orientation of its normal vector, the third eigenvector, X3, can thus be directly used to predict the orientation of the particle's plane.

Fig. 5 shows the adopted approach consisting in first finding the plane of the clay particle shown in Fig. 5a, based on the constituent points of the particle using the PCA method, then to determine the normal vector of the characterized plane.

The orientation of normal vectors is expressed by the system of angle (φ, θ) in the three-dimensional reference of the sub-sample, referenced previously with respect to the axis of the vertical one-dimensional compression stress. As depicted in the schematic representation of particle's normal vector by its local coordinates of the Fig. 5c, the latitude angle named φ, ranging from 0° to 90°, represents the angle formed by the normal vector and the positive *Z*-axis, while the longitude angle θ, ranging from 0° to 360°, is the angle of rotation around the Z-axis in the (XY) plane. These two angles are used to determine their frequency in

the analysis of particle orientations properties in the microvolume.

4.2. Filter Criterion to select particles representing the microvolume fabric

As previously demonstrated, the proposed clay particle reconstruction is greatly related to the segmentation method developed with AI, meaning that it needs to be validated in every use with great rigor. Thus, it appears as essential to further enhance the accuracy of the identification process. For instance, the SEM images sometimes showed zones of indistinguishable particles or that cannot be easily separated as shown in the example given in Fig. 6. Obviously, this kind of particle configuration can disturb the AI segmentation stage, and finally impact the clay fabric property analyses. Therefore, a filtering criterion is essential to be introduced in this approach.

Given the prior knowledge of the of kaolinite clay particle geometry, which typically exhibits platelet forms as explained in section 2.1, we propose a criterion based on this geometry data. The latter consists in firstly remove all particles smaller than 5000 voxels. Notice that this size-based filtering also helps eliminate small artifacts or noise that may have been misclassified as clay particles during the segmentation process. The watershed tool in Avizo software was then used to improve further the areas where particle individualization issue remains. After the separation stage, an additional improvement was implemented by removing particles smaller than 5000 voxels. Finally, the fabric of a micro-volume after individual identification of the reconstructed particles is obtained and represented in Fig. 7. Particles assigned with different colors mean that they have been individualized.

After the above first filter, still the shape of the clay particle which may play crucial role in its adequate identification. Indeed, platelet-shaped particles are more likely to be accurately identified. This data can be implicitly analyzed through the determined eigenvalues for each clay particle (particle plane discussed in §4.1), which represent the expansion of the particle's geometry along the corresponding eigenvector directions. In the case of planar-shaped particles, the third eigenvalue should be relatively small compared to the first and second eigenvalues. This tool allows to define the second criterion for particle selection which consists to consider the ratio of the smallest to the medium eigenvalues of the covariance matrix (λ_3/λ_2), representing the flatness parameter between 0 and 1. Flat objects have small values close to 0. Given that kaolinite particle has a lateral dimension between about 0.1 and 4 μm, and a thickness of about 0.05 to 2 μm (see for instance (Mitchell and Soga, 2005; Bandera et al., 2021)). One proposes to set the maximum flatness parameter at 10 %. This means that only particles with a flatness value below 10 % were consider for the orientation identification analysis. This criterion was imposed to the proposed analysis to ensure that the identified and retained geometries for normal calculation are flat and correspond as much as possible to the shape of the kaolinite particles, it on the other hand ensured adequate representativeness of the number of analyzed particles.

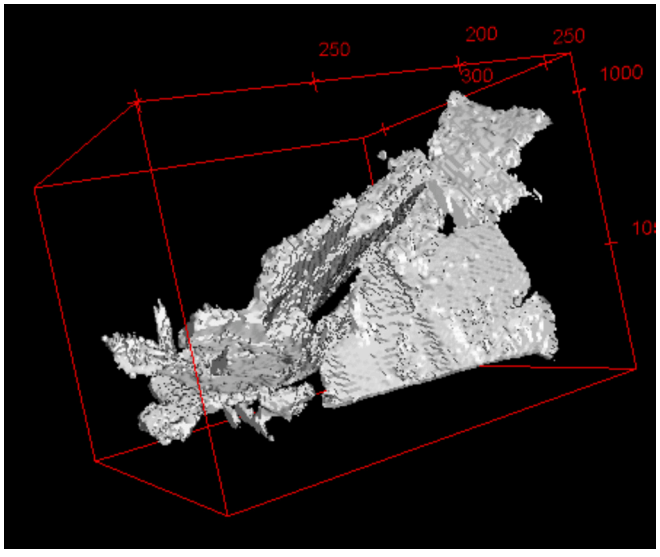

Fig. 6. Example of a poorly identified clay particle - A likely disrupt object visualization of the particle's orientation patterns

Fig. 8 illustrates three examples of particles after being submitted to classification criterion treatment, they exhibit a clear individual and planar particles. The proposed approach enhances the accuracy by specifically targeting particles with the desired platelet-like geometry. For this study, the criterion retained 12499 particles out of the initial 22260, ensuring a focus on particles with pronounced planar shape. Finally, one obtains highly appropriate system allowing to represent quite well the overall fabric of the micro-volume.

5. Mechanical loading and the induced microstructural properties from FIB-SEM reconstructed images

5.1. Basic conceptual diagrams for fabric interpretation

After the identification of the particles distributed in the micro-volume space explained in the above section, it becomes possible to quantify the orientation of the particles. One method consists of representing the orientations by the property's normal vectors, that is to say by their two angles, φ (latitude) and θ (longitude) (Fig. 5c). The latter can be represented in form of individual histograms as shown in Fig. 9a and Fig. 9b. In these figures, the latitude and longitude angles are represented versus their frequency. Notice that the latitude angle φ measures the inclination of a particle's normal vector relative to the z-axis representing the direction of axial (vertical) stress as illustrated in Fig. 5c.

$\varphi = 0^\circ$ indicates that the normal vector is parallel to the axial stress direction (*Z*-axis) with particles oriented towards horizontal plane parallel to [XY] plane. $\varphi = 90^\circ$ indicates that the normal vector is perpendicular to the axial stress direction. The θ angle represents the rotation of the normal vector in the [XY] plane (Fig. 5c) perpendicular to the vertical stress axis. Therefore, $\theta = 0^\circ$ corresponds to a normal vector parallel to the X-axis, with the particle being on the [YZ] plane. $\theta = 90^\circ$ corresponds to a normal vector perpendicular to the X-axis, with the particle being on the [XZ] plane.

The results of 3D orientation are represented as a spatial histogram in the form of a hemisphere, where the frequencies of the global orientations of the normal vectors are visualized using color intensity. A step size of 10 degrees was chosen for both the latitude and longitude angles, as shown in Fig. 9c. Dark red color indicates a high number of normal vectors oriented in a specific direction, while a dark blue color is assigned to cells where no vectors are detected in the given directions.

5.2. Particle orientations identification related to mechanical loading

Taken the case of a clay specimen under one-dimensional compression at $\sigma'_v = 120$ kPa, the highest frequencies are located in the φ range above 30° particularly between 30° and 60° (Fig. 9a). The diagram shows frequency peaks in θ angle variation within the range of 80° to 150° (Fig. 9b), outside this range, a uniform distribution is observed. This representation mode shows that the system exhibits a relative preferential arrangement of the particles.

The representation in form of hemispheres such as the one represented in Fig. 9c shows how the global distribution of normal vector orientations is inside the reconstructed micro-volume. Here, red graduations represent the latitude angle φ, while the dark graduations represent the longitude angle θ. The results show that the normal vectors tend to be more or less oriented towards localized directions, more precisely one obtains:

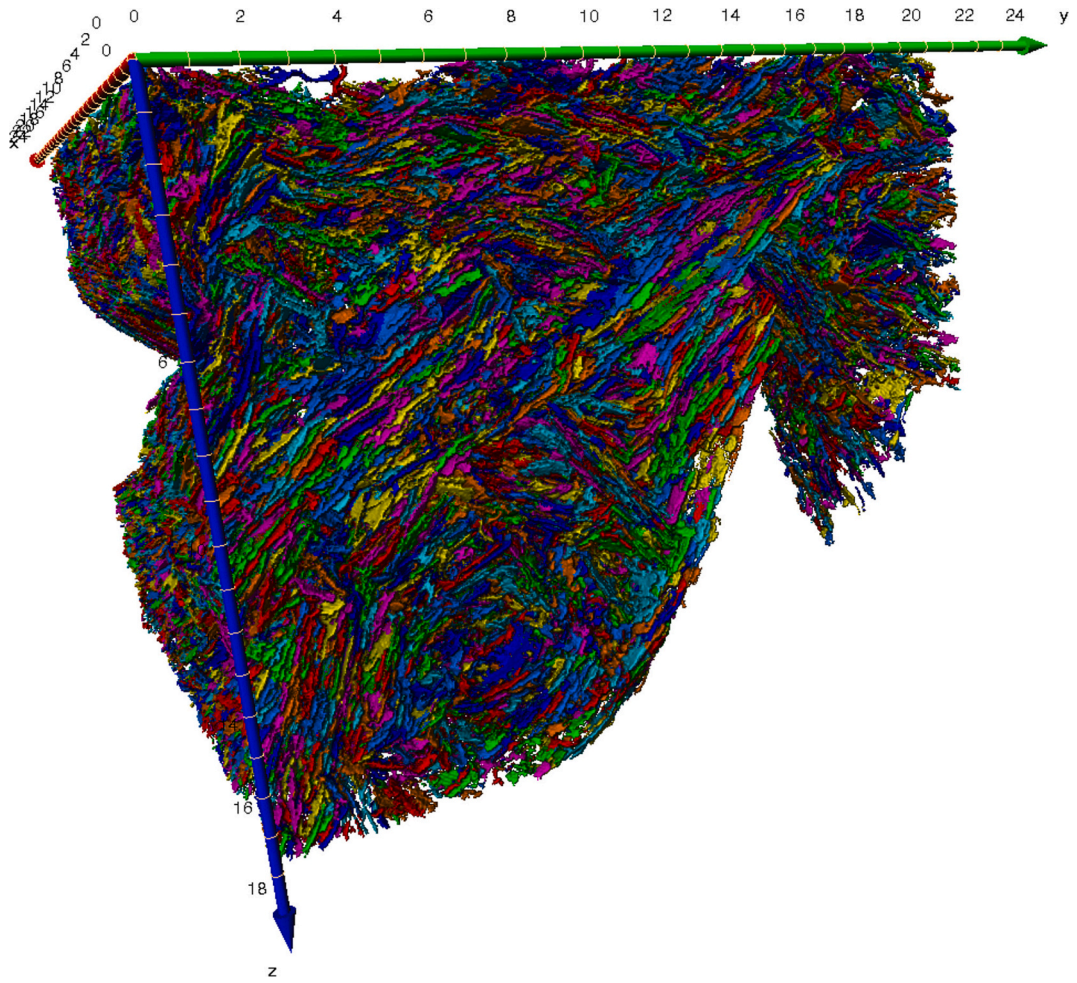

Fig. 7. Example of micro-volume fabric result after correcting the individual identification of the reconstructed particles.

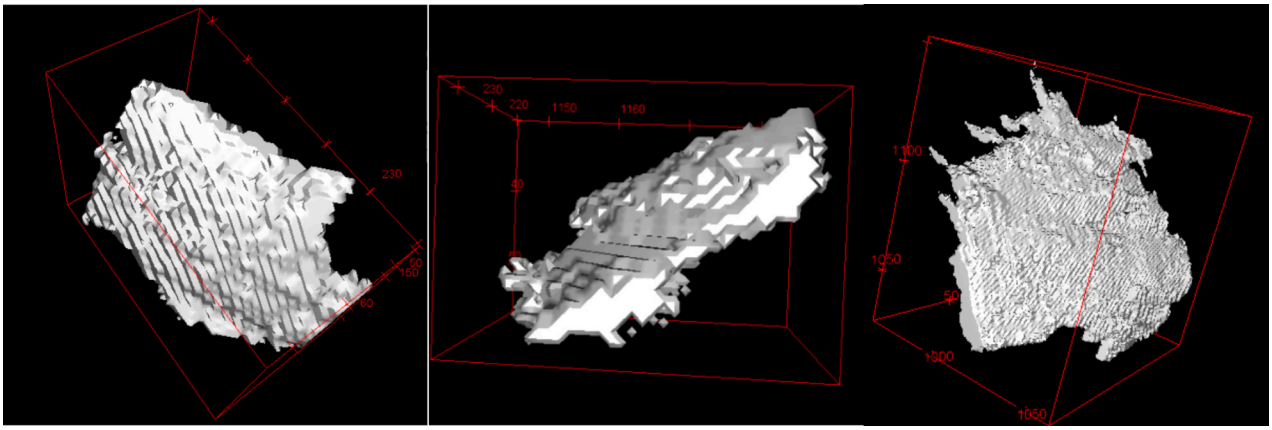

Fig. 8. Examples of 3D reconstruction models of three clay particles after applying a flatness parameter filter set at 10 %.

- Direction 1: located within the latitude angle interval $\varphi \in [30°, 40°]$ and the longitude angle interval $\theta \in [100°, 140°]$.
- Direction 2: located within the latitude angle interval $\varphi \in [40°, 50°]$ and the longitude angle interval $\theta \in [80°, 130°]$.
- Direction 3: located within the latitude angle interval $\phi \in [50°, 60°]$ and the longitude angle interval $\theta \in [100°, 110°]$.

5.3. Interpretation and discussion

To exploit the results mentioned above, a possible analysis would be to establish a connection between the dome of Fig. 9c and a geometry representing a perfect structural isotropy for a fictitious clay material, where particles described a random orientation. On other terms, a perfectly structural isotropy means all the cells of the hemisphere are uniformly distributed with an identical frequency, which is in this case equal to 0.308 %. Consequently, it becomes quite well feasible to

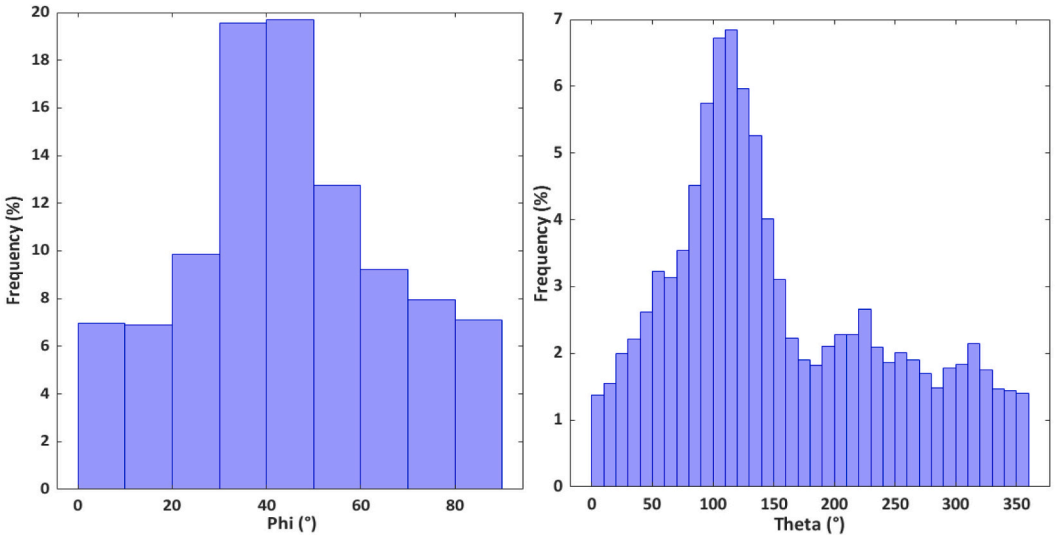

a. latitude angle ranges φ b. longitude angle ranges θ

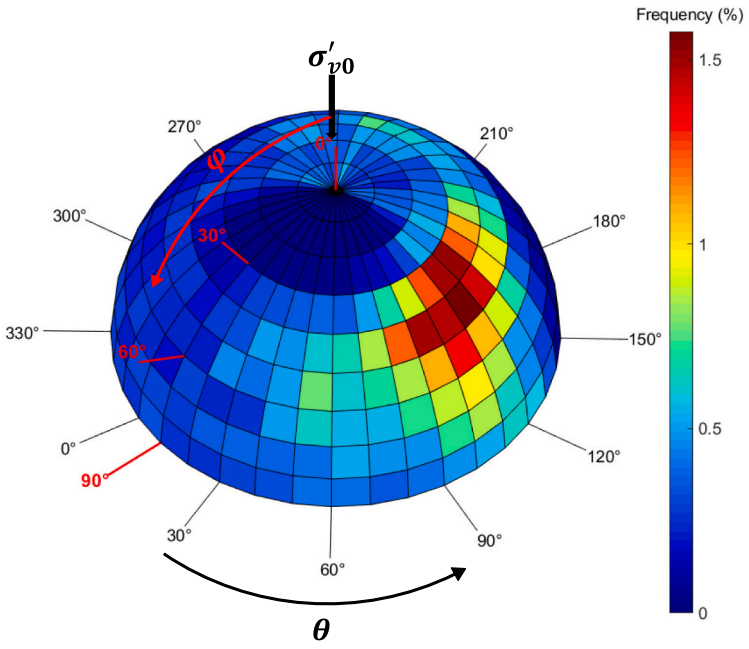

c. Hemisphere representation of the global orientation of normal vectors

Fig. 9. Orientation of the normal vectors after mechanical loading of the sample under one-dimensional compression (σ'v = 120 kPa)
a latitude angle ranges φ
b longitude angle ranges θ
c Hemisphere representation of the global orientation of normal vectors

identify the orientations of a group of normal vectors located within the range [30° to 60°], relative to the σ'_{v0} direction, by considering the intensities greater than the perfect isotropy threshold of 0.308 %.

One would have expected preferential orientations indicating particles arranged more or less towards the [XY] plane, the normal vectors being more or less parallel to the σ'_{v0} direction. However, the presence of numerous silica grains in the micro-volume (up to 13 µm edges) acting as obstacles prevent the free rotations of the clayey particles in response to mechanical loading. Fig. 10, which presents a particular zone of the micro-volume where are located several silica grains, helps to explain these results. The figure represents image slices within the micro-volume, they are located at different depths along the acquisition direction (X-axis): at 6 µm (slice 600 in Fig. 10b), 10 µm (slice 1000 in Fig. 10c), and 14 µm (slice 1400 in Fig. 10d). Each slice represents an image of the clay in the (YZ) plane (Fig. 10a).

These images reveal that in zones especially rich in silica grains, the loading in one-dimensional compression causes a flow of clay particles around the grains. This observation aligns well with that reported by Hattab (2011). This flow is clearly visible in the images, where particles are seen sliding in groups around the grains, thus conforming to their shape. Therefore, in the representation of the results in the hemisphere, certain cells will stand out from the others as clearly observed in Fig. 9c.

To reinforce this analysis, one may consider a cropped region of 8.01 µm thickness (Fig. 10a) from the micro-volume, delimited by the two

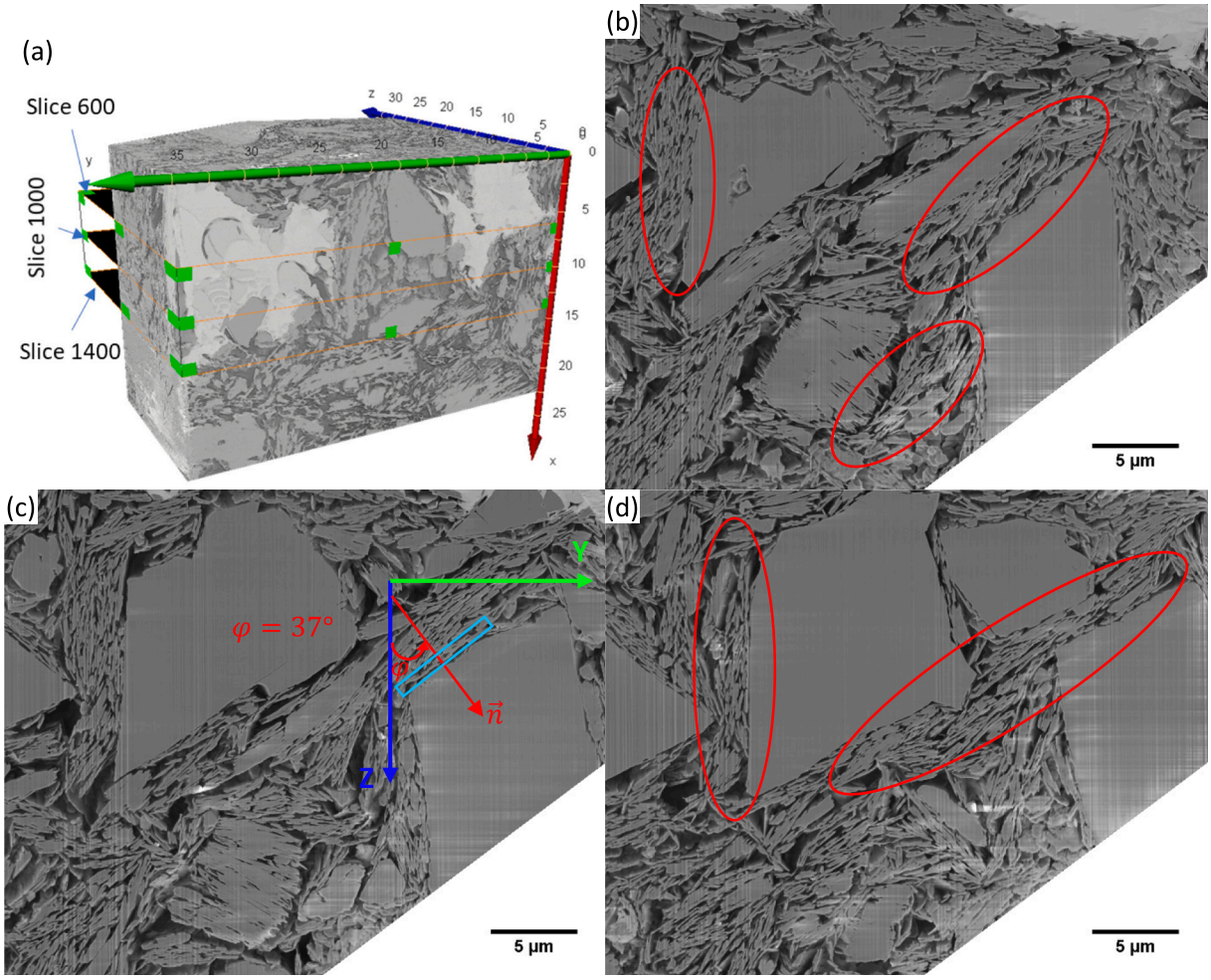

Fig. 10. View of silica grains at different depths within the sub-volume. a) volume extracted from the micro-volume, b) slice 600, c) slice 1000, and d) slice 1400.

silica grains located between 6 µm and 14 µm, where the orientation of the normal vectors of particle planes, neighboring the large grains, can be locally quantified. Fig. D. 15 presents the results of clay particle organization around large the silica grains. Hence, the fabric properties change compared to those of the entire micro-volume. Here, we can notice that significant concentration of normal vectors orientations is highlighted for a φ angle ranged [20°-50°] (Fig. D. 15a) associated with θ angle of [80°-150°] range (Fig. D. 15b). Indeed, compared to the global microvolume quantification, the magnitude of the preferential orientations towards to the above range increases dramatically, for instance by 14.55 % for φ angle, i.e. going from 49.32 % (at the micro-volume scale) to 63.87 % (at the cropped zone scale).

As consequence, with hemisphere type of representation (Fig. D. 15c), we can observe that the percentage of particles aligning between φ = 30° and φ = 70° becomes significantly higher compared to the results on the entire micro-volume case represented on Fig. 9c.

These results demonstrate again the power of the proposed method, which is also capable to bring with high accuracy a quantitative results of fabric properties well adapted to the scale of observation. However, it should be noted that the time required to carry out the various steps involved in achieving a comprehensive 3D microstructure analysis using the developed technique — from mechanical testing and sampling to the final results — is significant. This could be seen as a drawback of the technique.

6. Conclusion

This paper presents a study fully oriented towards experimental investigations, proposing a reliable methodology and a rigorous protocol using the 3D-SEM-FIB technique, which is novel for clayey material such as slightly consolidated mud-clays (at one-dimensional compression conditions in this paper). To achieve this, the approach follows a precise sequence of experimental steps, fully developed within the framework of this study. These steps include, first, an explanation of the experimental procedures, followed by 3D observations, and finally, image processing aimed at identifying the spatial organization of clay particles in relation to mechanical loading of the clay. Thus, a new method using machine learning to process 3D images was presented. By leveraging advanced machine learning tools and convex optimization algorithms, the spatial orientation of clay particles was successfully determined and linked to mechanical loading. The proposed AI-based segmentation approach, designed for accurately identifying platelet-shaped objects, was rigorously tested and validated using a thesis manuscript from the 60s, which demonstrated its effectiveness in identifying leaves.

Moving beyond traditional threshold segmentation methods, we adopted trained machine learning models for segmentation. This powerful approach generated probability maps, which were further filtered to exclusively select clay regions with a probability exceeding 95 %. To transform the segmented stack images into a comprehensive 3D model, we employed a 3D classification approach, followed by an analysis conducted using the Python programming language.

The properties of the reconstructed clay particles were determined

using principal component analysis (PCA) method to access the covariance matrix as well as its eigenvalues and eigenvectors. This approach provided valuable insights into the orientation of particle normal vectors, enabling an effective 3D representation within the global reference frame of the micro-volume.

Finally, the proposed approach, which aims to reconstruct the 3D microstructural state of a consolidated kaolinitic clay and analyze the spatial configuration of particles, leads to exploitable results with appreciable quality. The paper demonstrates how investigations, combined with the appropriate method of analysis, yield highly accurate quantitative results concerning fabric properties, well adapted to the scale of observation. The approach also appears capable of detecting and restoring local disturbances related to inclusions (such as silica grains), which modify the general trend in particle orientations.

CRediT authorship contribution statement

Ismail Myouri: Writing – review & editing, Writing – original draft, Visualization, Validation, Software, Resources, Investigation. **Fares Bennai:** Writing – review & editing, Writing – original draft, Visualization, Validation, Supervision, Software, Methodology, Investigation, Conceptualization. **Julien Guyon:** Writing – review & editing, Visualization, Investigation. **Mahdia Hattab:** Writing – review & editing, Writing – original draft, Visualization, Validation, Supervision, Project administration, Methodology, Investigation, Conceptualization.

Declaration of competing interest

The authors declare that they have no known competing financial interests or personal relationships that could have appeared to influence the work reported in this paper.

Appendix A. Appendix

Fig. A.11. SEM observation of clay particles.

Appendix B. Appendix

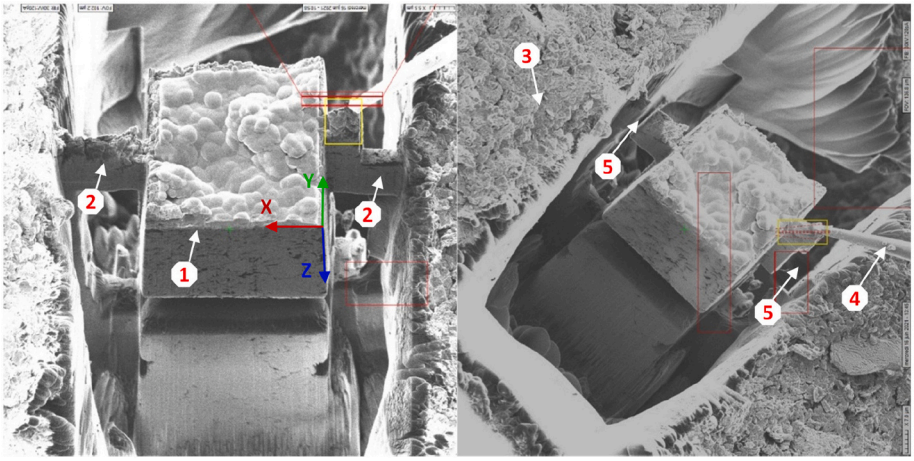

a. Selection of a suitable zone on the surface of clay sub-specimen and volume cutting using the ion beam

b. Attachment of the nanomanipulator to the micro-volume and removal of the remaining material

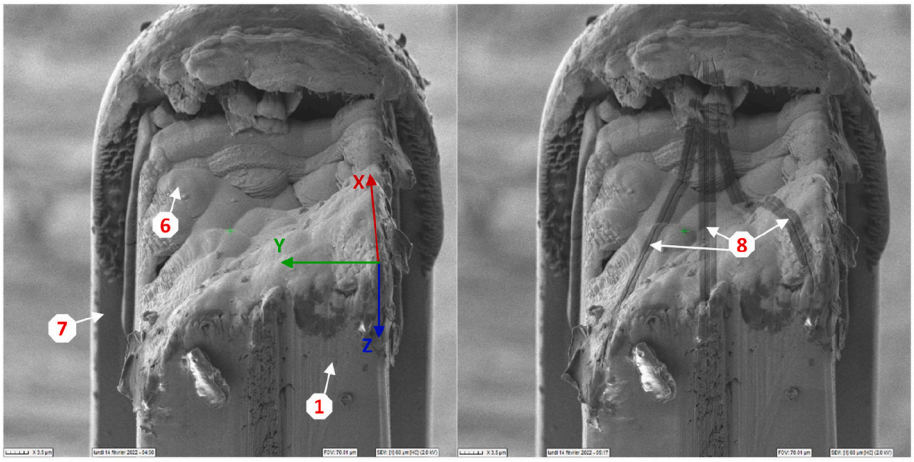

c. Deposition of the micro-volume onto a copper grid

d. Establishment of five lines of reference marks

Fig. B.12. Main steps of FIB-SEM technique.
Captions: (1) Micro-volume, (2) Two preserved points on parallel lateral surfaces maintain the micro-volume, (3) surface of the sub-specimen (4) nanomanipulator (5) Cutting of the material from the remaining two points (6) metallized surface of the micro-volume (7) copper support for TEM blade (8) Five lines of reference marks.

Appendix C. Appendix

	Image	Fourier Domain
	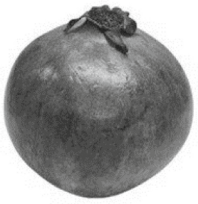 a. Original image	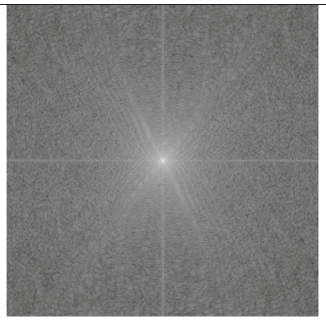 4b. FFT of original image
	 c. Image with striping noise	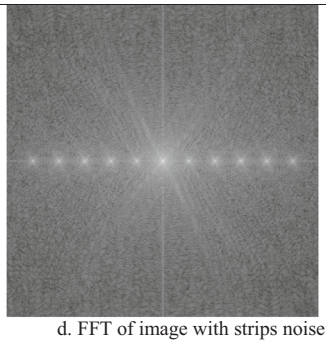 d. FFT of image with strips noise
	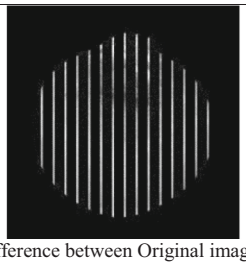 e. Difference between Original image and Image with strip noise	

Fig. C.13. Treatment: Image of a pomegranate before and after adding noise similar to the striping artifacts generated by the FIB-SEM technique

	Fourier Domain	Image
	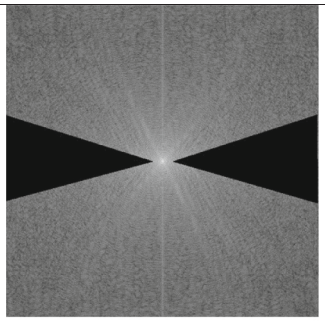 a. FFT of image with strips noise after wedge elimination	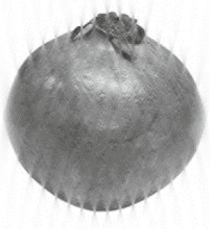 b. Denoised Image with Wedge elimination in Fourier Domain
		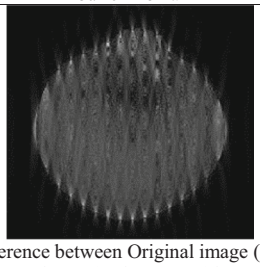 c. Difference between Original image (Fig. A. 15a) and Denoised Image with Wedge elimination in Fourier Domain (Fig. B. 16b)
	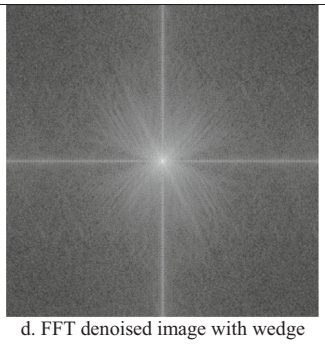 d. FFT denoised image with wedge elimination + Total variation reconstruction	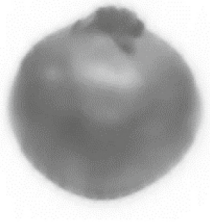 e. Denoised Image with Wedge elimination in Fourier Domain + Reconstruction of the image with total variation technique
		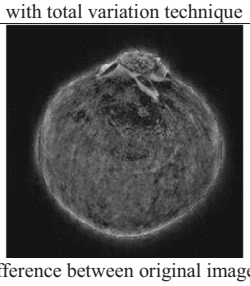 f. Difference between original image and denoised Image with Wedge elimination in Fourier Domain + Reconstruction of the image with total variation technique

Fig. C.14. Results and output: Image of a pomegranate after denoising and removal of curtain effects.

Appendix D. Appendix

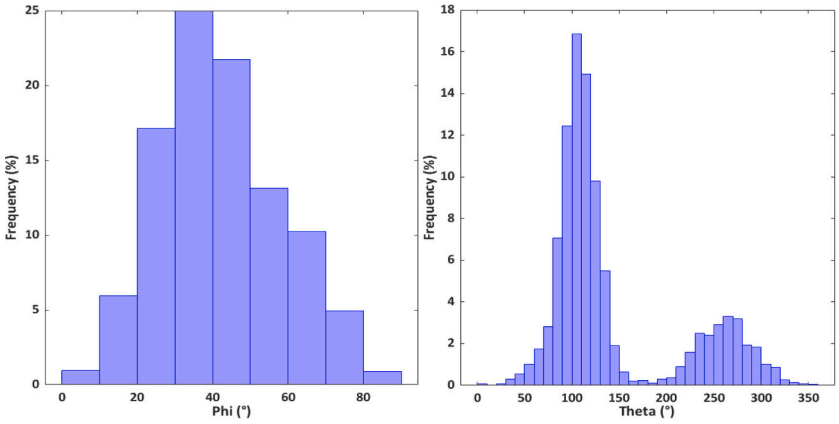

a. Histogram of latitude φ angle

b. Histogram of longitude θ angle

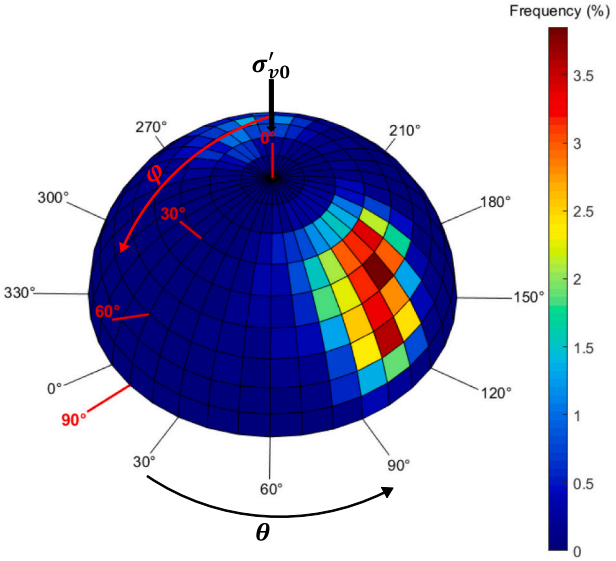

c. Hemisphere representation of the global orientation of normal vectors

Fig. D.15. Clay particle organization in space within a zone rich of large grains.

Appendix E. Supplementary data

Supplementary data to this article can be found online at https://doi.org/10.1016/j.clay.2025.107943.

Data availability

The data that has been used is confidential.

References

Al-Rawas, A.A., McGown, A., 1999. Microstructure of Omani expansive soils. Can. Geotech. J. 36, 272–290. https://doi.org/10.1139/t98-111.

Asaad, A., Hubert, F., Ferrage, E., Dabat, T., Paineau, E., Porion, P., Savoye, S., Gregoire, B., Dazas, B., Delville, A., Tertre, E., 2021. Role of interlayer porosity and particle organization in the diffusion of water in swelling clays. Appl. Clay Sci. 207, 106089. https://doi.org/10.1016/j.clay.2021.106089.

Bandera, S., O'Sullivan, C., Tangney, P., Angioletti-Uberti, S., 2021. Coarse-grained molecular dynamics simulations of clay compression. Comput. Geotech. 138, 104333. https://doi.org/10.1016/j.compgeo.2021.104333.

Benbouras, M.A., Lefilef, L., 2023. Progressive Machine Learning Approaches for predicting the Soil Compaction Parameters. Transp. Infrastruct. Geotech. 10, 211–238. https://doi.org/10.1007/s40515-021-00212-4.

Bennai, F., Bourbatache, M.K., Le, T.D., Hattab, M., Millet, O., 2025a. Determination of effective diffusion properties based on 3D FIB/SEM images of clays. Appl. Clay Sci. 267, 107717. https://doi.org/10.1016/j.clay.2025.107717.

Bennai, F., Hattab, M., Ding, Y., Jrad, M., Guyon, J., 2025b. Pore Network 3D Reconstruction for Clays using FIB-SEM Images. IOP Conf. Ser.: Earth Environ. Sci. 1480, 012079. https://doi.org/10.1088/1755-1315/1480/1/012079.

Biarez, J., Hicher, P.-Y., 1994. Elementary Mechanics of Soil Behaviour: Saturated Remoulded Soils. Balkema, Rotterdam.

Birmpilis, G., Dijkstra, J., Tudisco, E., Hall, S., 2017. In-situ study of deformation mechanisms of soft clay using X-ray Computed Tomography and Digital Volumetric Correlation. In: 3rd International Conference on Tomography of Materials and Structures, ICTMS2017-30. Lund, Sweden.

Birmpilis, G., Mohammadi, A.S., Villanova, J., Boller, E., Ando, E., Dijkstra, J., 2022. Fabric Investigation of Natural Sensitive Clay from 3D Nano- and Microtomography Data. J. Eng. Mech. 148, 04021151. https://doi.org/10.1061/(ASCE)EM.1943-7889.0002044.

Bordigoni, B., Trivellato, S., Pellegrini, R., Meregalli, S., Bonetto, E., Belmonte, M., Castellano, M., Panizza, D., Arcangeli, S., De Ponti, E., 2024. Automated segmentation in pelvic radiotherapy: a comprehensive evaluation of ATLAS-,

machine learning-, and deep learning-based models. Phys. Med. 125, 104486. https://doi.org/10.1016/j.ejmp.2024.104486.
Čalkovský, M., Müller, E., Meffert, M., Firman, N., Mayer, F., Wegener, M., Gerthsen, D., 2021. Comparison of segmentation algorithms for FIB-SEM tomography of porous polymers: Importance of image contrast for machine learning segmentation. Mater. Charact. 171, 110806. https://doi.org/10.1016/j.matchar.2020.110806.
Cetin, H., Söylemez, M., 2004. Soil-particle and pore orientations during drained and undrained shear of a cohesive sandy siltclay soil. Can. Geotech. J. 41, 1127–1138. https://doi.org/10.1139/t04-055.
Cheng, W.-Q., Yang, Z., Hattab, M., Bian, H., Bouchemella, S., Fleureau, J.-M., 2021. Free desiccation shrinkage process in clayey soils. Eur. J. Environ. Civ. Eng. 1–26. https://doi.org/10.1080/19648189.2021.1942223.
Chow, J.K., Li, Z., Wang, Y.-H., 2019. Comprehensive microstructural characterizations of 1-D consolidated kaolinite samples with fabric tensors and pore elongation factors. Eng. Geol. 248, 22–33. https://doi.org/10.1016/j.enggeo.2018.10.016.
Cotecchia, F., Cafaro, F., Guglielmi, S., 2016. Microstructural changes in Clays Generated by Compression Explored by Means of SEM and image Processing. Procedia Engineering 158, 57–62. https://doi.org/10.1016/j.proeng.2016.08.405.
Das, A., Chakrabortty, P., 2022. Simple models for predicting cyclic behaviour of sand in quaternary alluvium. Arab. J. Geosci. 15, 385. https://doi.org/10.1007/s12517-022-09639-6.
Delage, P., Lefebvre, G., 1984. Study of the structure of a sensitive Champlain clay and of its evolution during consolidation. Can. Geotech. J. 21, 21–35. https://doi.org/10.1139/t84-003.
Delage, P., Pellerin, F., 1984. Influence de la lyophilisation sur la structure d'une argile sensible du Québec. Clay Miner. 19, 151–160.
Diamond, S., 1971. Microstructure and Pore Structure of Impact-Compacted Clays. Clay Clay Miner. 19, 239–249. https://doi.org/10.1346/CCMN.1971.0190405.
Ding, Y., Bennai, F., Jrad, M., Guyon, J., Hattab, M., 2024. Three-dimensional pore network of kaolin using FIB-SEM imaging. Part. Sci. Technol. 42, 815–831. https://doi.org/10.1080/02726351.2023.2292271.
Dumoux, M., Glen, T., Smith, J.L., Ho, E.M., Perdigão, L.M., Pennington, A., Klumpe, S., Yee, N.B., Farmer, D.A., Lai, P.Y., Bowles, W., Kelley, R., Plitzko, J.M., Wu, L., Basham, M., Clare, D.K., Siebert, C.A., Darrow, M.C., Naismith, J.H., Grange, M., 2023. Cryo-plasma FIB/SEM volume imaging of biological specimens. eLife 12, e83623. https://doi.org/10.7554/eLife.83623.
Ellis, G.W., Yao, C., Zhao, R., Penumadu, D., 1995. Stress-Strain Modeling of Sands using Artificial Neural Networks. J. Geotech. Eng. 121, 429–435. https://doi.org/10.1061/(ASCE)0733-9410(1995)121:5(429).
Fan, W., Yang, P., Yang, Z., Joey, 2021. Freeze-thaw impact on macropore structure of clay by 3D X-ray computed tomography. Eng. Geol. 280, 105921. https://doi.org/10.1016/j.enggeo.2020.105921.
Fang, L., Seifert, S., Winans, R.E., Li, T., 2021. Operando XAS/SAXS: Guiding Design of Single-Atom and Subnanocluster Catalysts. Small Meth. 2001194. https://doi.org/10.1002/smtd.202001194.
Faÿ-Gomord, O., Soete, J., Davy, C.A., Janssens, N., Troadec, D., Cazaux, F., Caline, B., Swennen, R., 2017. Tight chalk: Characterization of the 3D pore network by FIB-SEM, towards the understanding of fluid transport. J. Pet. Sci. Eng. 156, 67–74. https://doi.org/10.1016/j.petrol.2017.05.005.
Fehrenbach, J., Weiss, P., Lorenzo, C., 2012. Variational Algorithms to Remove Stationary Noise: applications to Microscopy Imaging. IEEE Trans. on Image Process. 21, 4420–4430. https://doi.org/10.1109/TIP.2012.2206037.
Gaboreau, S., Robinet, J.-C., Prêt, D., 2016. Optimization of pore-network characterization of a compacted clay material by TEM and FIB/SEM imaging. Microporous Mesoporous Mater. 224, 116–128. https://doi.org/10.1016/j.micromeso.2015.11.035.
Gao, Q.-F., Hattab, M., Jrad, M., Fleureau, J.-M., Hicher, P.-Y., 2020a. Microstructural organization of remoulded clays in relation with dilatancy/contractancy phenomena. Acta Geotech. 15, 223–243. https://doi.org/10.1007/s11440-019-00876-w.
Gao, Q.-F., Jrad, M., Hattab, M., Fleureau, J.-M., Ameur, L.I., 2020b. Pore Morphology, Porosity, and Pore size distribution in Kaolinitic Remolded Clays under Triaxial Loading. Int. J. Geomech. 20, 04020057. https://doi.org/10.1061/(ASCE)GM.1943-5622.0001682.
Ghaboussi, J., Garrett, J.H., Wu, X., 1991. Knowledge-based Modeling of Material Behavior with Neural Networks. J. Eng. Mech. 117, 132–153. https://doi.org/10.1061/(ASCE)0733-9399(1991)117:1(132).
Giannuzzi, L.A., Stevie, F.A., 1999. A review of focused ion beam milling techniques for TEM specimen preparation. Micron 30, 197–204. https://doi.org/10.1016/S0968-4328(99)00005-0.
Giannuzzi, L.A., Stevie, F.A. (Eds.), 2005. Introduction to Focused Ion Beams: Instrumentation, Theory, Techniques and Practice. Springer US, Boston, MA. https://doi.org/10.1007/b101190.
Griffiths, F.J., Joshi, R.C., 1989. Change in pore size distribution due to consolidation of clays. Géotechnique 39, 159–167. https://doi.org/10.1680/geot.1989.39.1.159.
Hammad, T., Fleureau, J.-M., Hattab, M., 2013. Kaolin/montmorillonite mixtures behaviour on oedometric path and microstructural variations. Eur. J. Environ. Civ. Eng. 17, 826–840. https://doi.org/10.1080/19648189.2013.822428.
Hattab, M., 2011. Critical state notion and microstructural considerations in clays. Comptes Rendus Mécanique 339, 719–726. https://doi.org/10.1016/j.crme.2011.07.007.
Hattab, M., Chang, C.S., 2015. Interaggregate Forces and Energy potential effect on Clay Deformation. J. Eng. Mech. 141, 04015014. https://doi.org/10.1061/(ASCE)EM.1943-7889.0000898.
Hattab, M., Fleureau, J.-M., 2010. Experimental study of kaolin particle orientation mechanism. Géotechnique 60, 323–331. https://doi.org/10.1680/geot.2010.60.5.323.
Hattab, M., Fleureau, J.-M., 2011. Experimental analysis of kaolinite particle orientation during triaxial path. Int. J. Numer. Anal. Methods Geomech. 35, 947–968. https://doi.org/10.1002/nag.936.
Hattab, M., Hicher, P.-Y., 2004. Dilating behaviour of overconsolidated clay. Soils Found. 44, 27–40. https://doi.org/10.3208/sandf.44.4_27.
Hemes, S., Desbois, G., Urai, J.L., Schröppel, B., Schwarz, J.-O., 2015. Multi-scale characterization of porosity in Boom Clay (HADES-level, Mol, Belgium) using a combination of X-ray μ-CT, 2D BIB-SEM and FIB-SEM tomography. Microporous Mesoporous Mater. 208, 1–20. https://doi.org/10.1016/j.micromeso.2015.01.022.
Hemes, S., Desbois, G., Klaver, J., Urai, J.L., 2016. Microstructural characterisation of the Ypresian clays (Kallo-1) at nanometre resolution, using broad-ion beam milling and scanning electron microscopy. Neth. J. Geosci. 95, 293–313. https://doi.org/10.1017/njg.2016.16.
Hicher, P.Y., Wahyudi, H., Tessier, D., 1994. Microstructural analysis of strain localisation in clay. Comput. Geotech. 16, 205–222. https://doi.org/10.1016/0266-352X(94)90002-7.
Hicher, P.Y., Wahyudi, H., Tessier, D., 2000. Microstructural analysis of inherent and induced anisotropy in clay. Mechan. Cohesive-frictional Mater. 5, 341–371. https://doi.org/10.1002/1099-1484(200007)5:5<341::AID-CFM99>3.0.CO;2-C.
Holzer, L., Gasser, P., Muench, B., 2006. Quantification of capillary pores and hadley grains in cement paste using fib-nanotomography. In: Konsta-Gdoutos, M.S. (Ed.), Measuring, Monitoring and Modeling Concrete Properties. Springer Netherlands, Dordrecht, pp. 509–516. https://doi.org/10.1007/978-1-4020-5104-3_62.
Hubert, F., Bihannic, I., Prêt, D., Tertre, E., Nauleau, B., Pelletier, M., Demé, B., Ferrage, E., 2013. Investigating the Anisotropic Features of Particle Orientation in Synthetic Swelling Clay Porous Media. Clay Clay Miner. 61, 397–415. https://doi.org/10.1346/CCMN.2013.0610501.
Jiang, Y., Punjabi, K., Pierce, I., Knight, D., Yao, T., Steeden, J., Hughes, A.D., Muthurangu, V., Davies, R., 2025. A machine learning algorithm for creating isotropic 3D aortic segmentations from routine cardiac MR localizers. Magn. Reson. Imaging 115, 110253. https://doi.org/10.1016/j.mri.2024.110253.
Keller, L.M., Holzer, L., Wepf, R., Gasser, P., 2011. 3D geometry and topology of pore pathways in Opalinus clay: Implications for mass transport. Appl. Clay Sci. 52, 85–95. https://doi.org/10.1016/j.clay.2011.02.003.
Laribi, S., Jouffrey, B., Fleureau, J.-M., 2005. On observation of freeze-dried smectite plane views of nanolayers. Appl. Phys. Lett. 86, 231915. https://doi.org/10.1063/1.1946917.
Laurich, B., Urai, J.L., Nussbaum, C., 2017. Microstructures and deformation mechanisms in Opalinus Clay: insights from scaly clay from the Main Fault in the Mont Terri Rock Laboratory (CH). Solid Earth 8, 27–44. https://doi.org/10.5194/se-8-27-2017.
Lemmens, H.J., Butcher, A.R., Botha, P.W.S.K., 2011. FIB/SEM and SEM/EDX: a New Dawn for the SEM in the Core Lab?. In: Petrophysics - The SPWLA Journal of Formation Evaluation and Reservoir Description, 52, pp. 452–456.
Lim, S., Lee, H.-S., Kawashima, S., 2018. Pore structure refinement of cement paste incorporating nanosilica: Study with dual beam scanning electron microscopy/focused ion beam (SEM/FIB). Mater. Charact. 145, 323–328. https://doi.org/10.1016/j.matchar.2018.08.045.
Liu, D., Tian, Q., Yuan, P., Du, P., Zhou, Junming, Li, Y., Bu, H., Zhou, Jieyu, 2019. Facile sample preparation method allowing TEM characterization of the stacking structures and interlayer spaces of clay minerals. Appl. Clay Sci. 171, 1–5. https://doi.org/10.1016/j.clay.2019.01.019.
Loucks, R.G., Reed, R.M., Ruppel, S.C., Hammes, U., 2012. Spectrum of pore types and networks in mudrocks and a descriptive classification for matrix-related mudrock pores. Bulletin 96, 1071–1098. https://doi.org/10.1306/08171111061.
Ma, G., Guan, S., Wang, Q., Feng, Y.T., Zhou, W., 2022. A predictive deep learning framework for path-dependent mechanical behavior of granular materials. Acta Geotech. 17, 3463–3478. https://doi.org/10.1007/s11440-021-01419-y.
Ma, M., Bennai, F., Hattab, M., Hicher, P.-Y., Nicot, F., 2025. The Interplay of Clay Behavior and Particle Structuring: a Multiscale Investigation. IOP Conf. Ser.: Earth Environ. Sci. 1480, 012096. https://doi.org/10.1088/1755-1315/1480/1/012096.
Manafi Khajeh Pasha, S., Hazarika, H., Yoshimoto, N., 2019. A Machine Learning Approach for Predicting Dynamic Characteristics of Granular Mixtures. In: Geotechnical Engineering in the XXI Century: Lessons Learned and Future Challenges. IOS Press, pp. 2017–2026.
Martin, R.T., Ladd, C.C., 1975. Fabric of Consolidated Kaolinite. Clay Clay Miner. 23, 17–25. https://doi.org/10.1346/CCMN.1975.0230103.
Mitchell, J.K., 1956. The fabric of natural clays and its relation to engineering properties. Proc. Highway Research Board 35, 693–713.
Mitchell, J.K., Soga, K., 2005. Fundamentals of Soil Behavior, 3rd ed. John Wiley & Sons, Hoboken, N.J.
Moayedi, H., Hayati, S., 2018. Modelling and optimization of ultimate bearing capacity of strip footing near a slope by soft computing methods. Appl. Soft Comput. 66, 208–219. https://doi.org/10.1016/j.asoc.2018.02.027.
Morgenstern, N.R., Tchalenko, J.S., 1967. Microscopic Structures in Kaolin Subjected to Direct Shear. Géotechnique 17, 309–328. https://doi.org/10.1680/geot.1967.17.4.309.
Murphy, C.P., Bullock, P., Biswell, K.J., 1977. The measurement and characterisation of voids in soil thin sections by image analysis. Part II applications. J. Soil Sci. 28, 509–518. https://doi.org/10.1111/j.1365-2389.1977.tb02259.x.
Nishimura, S., Okajima, S., Joshi, B.R., Higo, Y., Tokoro, T., 2020. Volumetric behaviour of clays under freeze–thaw cycles in a mesoscopically uniform element. Géotechnique 1–15. https://doi.org/10.1680/jgeot.20.P.047.

Nyo, M.T., Mebarek-Oudina, F., Hlaing, S.S., Khan, N.A., 2022. Otsu's thresholding technique for MRI image brain tumor segmentation. Multimed. Tools Appl. 81, 43837–43849. https://doi.org/10.1007/s11042-022-13215-1.

Pedrotti, M., Tarantino, A., 2018. An experimental investigation into the micromechanics of non-active clays. Géotechnique 68, 666–683. https://doi.org/10.1680/jgeot.16.P.245.

Pusch, R., 1970. Microstructural changes in soft quick clay at failure. Can. Geotech. J. 7, 1–7. https://doi.org/10.1139/t70-001.

Qi, H., Chen, Z., Zhou, L., 2015. CT image Reconstruction from Sparse Projections using Adaptive TpV Regularization. Comput. Math. Methods Med. 2015, 1–8. https://doi.org/10.1155/2015/354869.

Schwartz, J., Jiang, Y., Wang, Y., Aiello, A., Bhattacharya, P., Yuan, H., Mi, Z., Bassim, N., Hovden, R., 2019. Removing Stripes. In: Scratches, and Curtaining with Non-Recoverable Compressed Sensing. https://doi.org/10.48550/ARXIV.1901.08001.

Shalizi, C.R., 2013. Advanced Data Analysis from an Elementary Point of View, 2013. ed. Cambridge University Press.

Simms, P.H., Yanful, E.K., 2004. A discussion of the application of mercury intrusion porosimetry for the investigation of soils, including an evaluation of its use to estimate volume change in compacted clayey soils. Géotechnique 54, 421–426. https://doi.org/10.1680/geot.2004.54.6.421.

Singh, S., Mittal, N., Thakur, D., Singh, H., Oliva, D., Demin, A., 2022. Nature and Biologically inspired image Segmentation Techniques. Arch Computat Methods Eng 29, 1415–1442. https://doi.org/10.1007/s11831-021-09619-1.

Sivakumar, V., Doran, I.G., Graham, J., 2002. Particle orientation and its influence on the mechanical behaviour of isotropically consolidated reconstituted clay. Eng. Geol. 66, 197–209. https://doi.org/10.1016/S0013-7952(02)00040-6.

Sloane, R.L., 1966. The fabric of Mechanically Compacted Kaolin. Clay Clay Miner. 14, 289–296. https://doi.org/10.1346/CCMN.1966.0140125.

Song, Y., Davy, C.A., Troadec, D., Bourbon, X., 2019. Pore network of cement hydrates in a High Performance Concrete by 3D FIB/SEM — Implications for macroscopic fluid transport. Cem. Concr. Res. 115, 308–326. https://doi.org/10.1016/j.cemconres.2018.08.004.

Souli, H., Fleureau, J.-M., Trabelsi Ayadi, M., Kbir-Ariguib, N., 2010. A mineralogical identification of a Tunisian clayey soil and fabric changes during wetting. Clay Miner. 45, 315–326. https://doi.org/10.1180/claymin.2010.045.3.315.

Spehner, D., Steyer, A.M., Bertinetti, L., Orlov, I., Benoit, L., Pernet-Gallay, K., Schertel, A., Schultz, P., 2020. Cryo-FIB-SEM as a promising tool for localizing proteins in 3D. J. Struct. Biol. 211, 107528. https://doi.org/10.1016/j.jsb.2020.107528.

Tarantino, A., De Col, E., 2008. Compaction behaviour of clay. Géotechnique 58, 199–213. https://doi.org/10.1680/geot.2008.58.3.199.

Xin, J., Akiyama, M., Frangopol, D.M., 2024. Autonomous detection of steel corrosion spatial variability in reinforced concrete using X-ray technology and deep learning-based semantic segmentation. Autom. Constr. 158, 105252. https://doi.org/10.1016/j.autcon.2023.105252.

Yoshinaka, R., Kazama, H., 1973. Micro-Structure of Compacted Kaolin Clay. Soils Found. 13, 19–34. https://doi.org/10.3208/sandf1972.13.2_19.

Zhao, D., Hattab, M., Yin, Z.-Y., Hicher, P.-Y., 2019. Dilative behavior of kaolinite under drained creep condition. Acta Geotech. 14, 1003–1019. https://doi.org/10.1007/s11440-018-0686-x.

Zhao, D., Gao, Q.-F., Hattab, M., Hicher, P.-Y., Yin, Z.-Y., 2020. Microstructural evolution of remolded clay related to creep. Transportat. Geotechn. 24, 100367. https://doi.org/10.1016/j.trgeo.2020.100367.

Zhou, S., Yan, G., Xue, H., Guo, W., Li, X., 2016. 2D and 3D nanopore characterization of gas shale in Longmaxi formation based on FIB-SEM. Mar. Pet. Geol. 73, 174–180. https://doi.org/10.1016/j.marpetgeo.2016.02.033.